Icarus 293 (2017) 132–156

Contents lists available at ScienceDirect

Icarus

journal homepage: www.elsevier.com/locate/icarus

Vertical profiles of Mars 1.27 μm O_2 dayglow from MRO CRISM limb spectra: Seasonal/global behaviors, comparisons to LMDGCM simulations, and a global definition for Mars water vapor profiles

R. Todd Clancy[a,*], Michael D. Smith[b], Franck Lefèvre[c], Timothy H. McConnochie[e], Brad J. Sandor[a], Michael J. Wolff[a], Steven W. Lee[a,d], Scott L. Murchie[f], Anthony D. Toigo[f], Hari Nair[f], Thomas Navarro[g]

[a] Space Science Institute, 4750 Walnut Street, Suite 205, Boulder, CO 80301, UCB 564, United States
[b] NASA Goddard Space Flight Center, Greenbelt, MD 20771, United States
[c] Laboratoire Atmosphères Milieux Observations Spatiales, Paris, France
[d] Denver Museum of Nature and Science, Denver, CO, 80205, USA
[e] Department of Astronomy, University of Maryland, College Park, MD 20742, USA
[f] John Hopkins University Applied Physics Laboratory, Columbia, MD 20723, USA
[g] Laboratoire de Météorologie Dynamique, Paris, France

ARTICLE INFO

Article history:
Received 6 November 2016
Revised 16 April 2017
Accepted 17 April 2017
Available online 19 April 2017

ABSTRACT

Since July of 2009, The Compact Reconnaissance Imaging Spectral Mapper (CRISM) onboard the Mars Reconnaissance Orbiter (MRO) has periodically obtained pole-to-pole observations (i.e., full MRO orbits) of limb scanned visible/near IR spectra ($\lambda = 0.4 - 4.0$ μm, $\triangle\lambda \sim 10$ nm- Murchie et al., 2007). These CRISM limb observations support the first seasonally and spatially extensive set of Mars 1.27 μm $O_2(^1\triangle_g)$ dayglow profile retrievals ($\sim$ 1100) over $\geq$ 8–80 km altitudes. Their comparison to Laboratoire de Météorologie Dynamique (LMD) global climate model (GCM) simulated $O_2(^1\triangle_g)$ volume emission rate (VER) profiles, as a function of altitude, latitude, and season (solar longitude, L_s), supports several key conclusions regarding Mars atmospheric water vapor (which is derived from $O_2(^1\triangle_g)$ emission rates), Mars O_3, and the collisional de-excitation of $O_2(^1\triangle_g)$ in the Mars CO_2 atmosphere. Current (Navarro et al., 2014) LMDGCM simulations of Mars atmospheric water vapor fall 2–3 times below CRISM derived water vapor abundances at 20–40 km altitudes over low-to-mid latitudes in northern spring (L_s = 30-60°), and northern mid-to-high latitudes over northern summer (L_s = 60–140°). In contrast, LMDGCM simulated water vapor is 2–5 times greater than CRISM derived values at all latitudes and seasons above 40 km, within the aphelion cloud belt (ACB), and over high-southern to mid-southern latitudes in southern summer (L_s = 190-340°) at 15–35 km altitudes. Overall, the solstitial summer-to-winter hemisphere gradients in water vapor are reversed between the LMDGCM modeled versus the CRISM derived water vapor abundances above 10–30 km altitudes. LMDGCM-CRISM differences in water vapor profiles correlate with LMDGCM-CRISM differences in cloud mixing profiles; and likely reflect limitations in simulating cloud microphysics and radiative forcing, both of which restrict meridional transport of water from summer-to-winter hemispheres on Mars (Clancy et al., 1996; Montmessin et al., 2004; Steele et al., 2014; Navarro et al., 2014) and depend on uncertain cloud microphysical properties (Navarro et al., 2014). The derived low-to-mid latitude changes in Mars water vapor vertical distributions should reduce current model-data disagreements in column O_3 and H_2O_2 abundances over low-to-mid latitudes (e.g., within the ACB; Lefèvre et al., 2008; Encrenaz et al., 2015; Clancy et al., 2016). Lastly, the global/seasonal average comparison of CRISM and LMDGCM $O_2(^1\triangle_g)$ VER below 20 km altitudes indicates a factor of $\sim$3 times lower value (0.25×10^{-20} $cm^3 sec^{-1}$) for the CO_2 collisional de-excitation rate coefficient of $O_2(^1\triangle_g)$ than derived recently by Guslyakova et al. (2016).

* Corresponding author.
E-mail address: clancy@spacescience.org (R. Todd Clancy).

http://dx.doi.org/10.1016/j.icarus.2017.04.011
0019-1035/

1. Introduction

Near-infrared 1.27 μm band emission by electronically excited O_2 ($O_2(^1\Delta_g)$) in the Mars atmosphere was first detected by Noxon et al. (1976), who associated it with the photolysis (and hence spatial distribution) of Mars atmospheric ozone (O_3). Mars O_3 is strongly anti-correlated with Mars atmospheric water vapor (Barth et al., 1973), through its catalytic destruction by radical HO_x (OH, HO_2, H) products of water vapor photolysis (Parkinson and Hunten, 1972; McElroy and Donahue, 1972). The seasonal and spatial variabilities of Mars atmospheric water (vapor and ice) are, in turn, largely controlled by saturation conditions (e.g., Farmer et al., 1977; Clancy et al., 1996) such that atmospheric temperatures strongly influence the seasonal and spatial dependence of Mars $O_2(^1\Delta_g)$ dayglow.

1.1. Mars $O_2(^1\Delta_g)$ dayglow observations

Subsequent observations of Mars $O_2(^1\Delta_g)$ dayglow from both ground-based (Krasnopolsky and Bjoraker, 2000; Novak et al., 2002; Krasnopolsky, 2003; 2007) and spacecraft experiments (Fedorova et al., 2006; Altieri et al., 2009) explored comparisons among observed and modeled $O_2(^1\Delta_g)$ spatial and seasonal variations in the context of atmospheric water distributions and dynamical temperature perturbations. In particular, Guslyakova et al. (2016) present the seasonal and latitudinal distribution of extended SPICAM column $O_2(^1\Delta_g)$ measurements in the context of contemporaneous SPICAM water and O_3 column measurements and LMDGCM simulated $O_2(^1\Delta_g)$ columns.

Existing observations of Mars $O_2(^1\Delta_g)$ dayglow have emphasized nadir or column integrated measurements, as limb profiling near-infrared spectroscopy has only recently been available from the Mars Express (MEx) SPICAM (Fedorova et al., 2012) and OMEGA (Bertaux et al., 2012) experiments and the MRO CRISM experiment (Clancy et al., 2012; 2013b). Published MEx and MRO limb profiling observations have primarily addressed polar nightglow rather than dayglow $O_2(^1\Delta_g)$ measurements. Polar $O_2(^1\Delta_g)$ nightglow reflects high altitude (40–70 km) production by atomic oxygen recombination ($O + O + CO_2 \rightarrow O_2(^1\Delta_g) + CO_2$), a very distinct process indicative of upper level meridional transport rather than O_3/water vapor distributions. However, Guslyakova et al. (2014) have reported results for SPICAM $O_2(^1\Delta_g)$ dayglow limb measurements. SPICAM obtained limited spatial resolution at the atmospheric limb (typically poorer than 30 km) and the limb radiance analysis neglects aerosol extinction, limiting conclusions with model comparisons. Nevertheless, Guslyakova et al. (2014) demonstrate the potential of $O_2(^1\Delta_g)$ limb profiles to assess current uncertainties in Mars water vapor profile distributions in season and latitude, as well as $O_2(^1\Delta_g)$ molecular physics.

1.2. Mars O_3 observations and photochemistry

Direct measurements of Mars atmospheric ozone are much more extensive (e.g.; Barth et al., 1973; Fast et al., 2006; Perrier et al., 2006; Lefèvre et al., 2015a; Clancy et al., 2016), but have also been largely restricted to column measurements with the notable exception of nightside profile retrievals from SPICAM stellar occultation observations (Lebonnois et al., 2006). Model simulations for Mars O_3 indicate broad areas of agreement with existing O_3 observations. These include maximum column abundances over polar latitudes (Perrier et al., 2006) and southern mid-latitude basins (Hellas and Argyre, Clancy et al., 2016) in fall-winter-spring seasons, and low latitude O_3 increases above 10 km altitudes around Mars aphelion in northern summer (Clancy and Nair, 1996; Lefèvre et al., 2004; Lebonnois et al., 2006). However, several key areas of model-data disagreement are also noted. In particular, Mars global circulation models (MGCM) that simulate the 3D distribution of atmospheric water vapor tend to underestimate observed O_3 columns by as much as a factor-of-two at high and low latitudes (Lefèvre et al., 2004; 2008). Portions of this model-data disagreement reflect unknown vertical distributions for water vapor and O_3 as a function of season and latitude, as well as difficulties in simulating observed water column abundances versus latitude and season (Navarro et al., 2014). Heterogeneous chemistry on Mars clouds may also contribute to differences between modeled and observed O_3 columns at high latitudes (Lefèvre et al., 2008), although such chemistry remains uncertain (Clancy et al., 2016).

1.3. CRISM $O_2(^1\Delta_g)$ dayglow observations and water vapor determinations

The following presentation of CRISM profile retrievals for $O_2(^1\Delta_g)$ volume emission rates (VER) provides a unique opportunity to assess the daytime vertical distribution of Mars O_3 as a function of latitude and season (solar longitude, L_s), in the context of MGCM O_3 profile simulations. Such vertical coverage is particularly important in assessing the role of the poorly constrained global vertical distribution of Mars water vapor, as affected by seasonally and latitudinally dependent saturation conditions. The enhanced sensitivity of limb sounding (~60x nadir path lengths), in conjunction with this vertical profile retrieval capability, promotes important new insights into model versus observationally derived water vapor distributions over the extended 10–60 km altitude range as a function of season (L_S), latitude, and (to a lesser extent) longitude. These distributions bear on existing model-data disagreements in column O_3 (Lefèvre et al., 2008) and H_2O_2 (Encrenaz et al., 2015), as well as the global transport of water vapor. Distinctions between observed and modeled $O_2(^1\Delta_g)$ emission at altitudes below 10–20 km further support unique constraints on uncertain de-excitation rates associated with CO_2 collisions.

2. CRISM limb $O_2(^1\Delta_g)$ observations

CRISM is an visible-near infrared (λ=0.4–4 μm, 7–15 nm resolution) imaging spectrometer, designed to map Mars surface mineralogy at high spatial resolution (15–20 m/pixel) from the MRO near-polar, sun synchronous orbit (local time, LT, ~3pm/3am). Specific capabilities and early science results from the CRISM experiment may be found in Murchie et al. (2007; 2009). CRISM is nominally operated in the nadir, with gimbaling in track to improve signal-to-noise ratios (Murchie et al., 2007), spatial resolution (Coman et al., 2013), and support atmospheric aerosol measurements via emission-phase-function (EPF) measurements (Wolff et al., 2009).

2.1. CRISM limb observation coverages

Beginning in 2009, CRISM limb observations have been obtained through MRO spacecraft yaw maneuvers roughly every 30° of Mars solar longitude (L_S), although with numerous interruptions associated with MRO safings or other spacecraft considerations (see Table 1). These MRO yaws place the CRISM field-of-view (fov) at the atmospheric limb in the plane of the MRO orbit, the CRISM gimbal provides atmospheric limb scanning from the surface to altitudes above 110–130 km (Clancy et al., 2012). The CRISM limb imaging resolution, as set by spatial pixel binning along the limb and image summing in the vertical scan direction, is ~0.5 km. However, as described below, the limb radiative transfer (RT) retrievals generate $O_2(^1\Delta_g)$ volume emission rate (VER) profiles with ~3 km vertical resolution, which are subsequently interpolated to a standard 4 km aeroid altitude grid. This approach reflects the weakness of the Mars $O_2(^1\Delta_g)$ emission in comparison to

Table 1
CRISM limb $O_2(^1\triangle_g)$ dayglow observation summary (each entry is one full orbit of observations).

Date[a]	Year[b]	MY[c]	L_S[d]	Longitudes[e]	Latitudes[f]
July 10,11	2009	29	301°	H,T	88S–56N
February 10,11	2010	30	50°	T	51S–85N
April 7	2010	30	74°	H,T	42S–87N
April 28,29	2010	30	83–84°	H,T	43S–87N
May 26	2010	30	96°	H,T	39S–86N
August 22,23	2010	30	137°	0,100–210W	50S–25S
August 22,23	2010	30	137°	0,100–140W	41N–84N
October 17	2010	30	166°	H,T	64S–82N
December 5,6	2010	30	193°	H,T	83S–63N
March 31–April 1	2011	30	265°	H,T	87S–39N
May 14,15	2011	30	292–293°	H,T	86S–44N
June 28,	2011	30	319°	H,T	85S–52N
August 22,23	2011	30	349°	H,T	81S–65N
September 13	2011	31	0°	H,T	76S–70N
December 10,11	2011	31	41–42°	H,T	54S–87N
April 24,26	2012	31	101–102°	H,T,M	40S–86N
November 14–16	2012	31	206–208°	H,M,V	84S–64N
January 8,9	2013	31	241°	M,V	87S–47N
March 7	2013	31	277°	H	75S–19S
December 11,13	2013	32	61–62°	M,V	38S–87N
February 5,6	2014	32	86°	H,V	27S–86N
April 1–3	2014	32	110–111°	H,M,V	36S–81N
May 26–28	2014	32	136–137°	H,M,V	37S–85N
July 20,22,26	2014	32	164–167°	H,M,V	54S–86N
February 13,14	2015	32	290–291°	H,M	79S–48N
April 15,17	2015	32	326–327°	H,M,V	86S–66N
August 31, September 1,4	2015	33	35–37°	H,M,V	48S–86N
October 25,30–31	2015	33	59–62°	H,M,V	37S–80N
December 20,23,25	2015	33	84–86°	H,M,V	33S–85N
February 28, March 5,6	2016	33	115–118°	H,M,V	34S–87N
May 10,11,15	2016	33	150–153°	H,M,V	47S–87N
July 3,5,6	2016	33	179–181°	H,M,V	65S–83N
August 30	2016	33	213°	H	83S–3N
December 21	2016	33	284°	M	87S–56N

[a] Day/Month of CRISM orbit of observations.
[b] Year of CRISM orbit of observations.
[c] Mars Year of CRISM orbit of observations, as in Clancy et al. (2000).
[d] Mars Solar Longitude (90° for northern summer solstice, 70° for aphelion).
[e] EQ Longitude of CRISM orbit of observations (H∼ 295W, T∼ 105W, M∼ 0W, V∼ 75W).
[f] ∫Latitudinal Coverage of CRISM orbit of observations (at 6–12° latitude intervals).

the CRISM sensitivity, and the need to create a consistent vertical grid for global/seasonal comparisons among CRISM and LMDGCM model $O_2(^1\triangle_g)$ VER.

CRISM limb observations are typically performed over 2–3 full orbits observed within a 1–5 day period every 2–3 months. This leads to full latitudinal coverage from each orbit of observation, including substantial nightside coverage that has supported previous studies of Mars polar $O_2(^1\triangle_g)$ (Clancy et al., 2012; 2013b) and OH (Clancy et al., 2013a) nightglow studies. For the current $O_2(^1\triangle_g)$ dayglow study, day-lit latitudinal coverage extends from winter midlatitudes (30–50°) to summer polar latitudes including substantial morning (AM) coverage over the poles. The latitudinal sampling varies with altitude and latitude along the day-lit orbital range due to the altitude gimbal scanning pattern, but generally leads to 6–12° latitudinal offsets between limb scans.

The longitudinal coverage is limited to 2–4 selected longitudes of interest, centered on Hellas Basin (H-295W), the Tharsis ridge (T-105W), Meridiani (M-0W), and Valles Marineris (V-75W). Longitudes here refer to the equatorial (EQ) crossing of the orbit, and change considerably at very high latitudes (particularly over the poles) due to the slightly inclined MRO polar orbit. As apparent in Table 1, the longitudes of CRISM limb viewing were limited to 2 orbits centered on Hellas and Tharsis regions over 2009–2011 and then modified to 3 orbits centered on Hellas, Meridiani, and Valles Marineris from 2012 to 2016. The latter two longitude regions correspond to peak occurrences of mesospheric (55–75 km) CO_2 ice clouds, which are particularly well characterized by CRISM visible-to-near infrared spectra in limb viewing (Clancy et al., 2015). In fact, the cold conditions associated with such clouds lead to CRISM detections of distinct mesospheric $O_2(^1\triangle_g)$ emissions at 60–75 km (Clancy et al., 2015), to be addressed in a subsequent paper. Here, we restrict presented retrievals to altitudes below 60 km, with a focus on lower atmospheric O_3 and H_2O profile behaviors via LMDGCM comparisons.

2.2. CRISM $O_2(^1\triangle_g)$ limb emission characteristics

The CRISM spectral resolution does not afford resolution of the $O_2(^1\triangle_g)$ band structure, as demonstrated in Fig. 1 [modified from Clancy et al. (2012)]. Rather, a band integrated signal is obtained in three CRISM channels centered on the 1.27 μm band structure, and adjoining background channels on either side are employed to isolate the $O_2(^1\triangle_g)$ emission from aerosol scattering. These $O_2(^1\triangle_g)$ channel selections are indicated in Fig. 1, as is the Gaussian weighting of the CRISM channels near 1.27 μm. Fig. 1 also presents weak and strong $O_2(^1\triangle_g)$ emissions captured in May 2016 (L_S=152°) CRISM limb spectra, as summed for limb tangent altitudes over 22–25 km. In this presentation, the broad limb brightness continuum associated with atmospheric aerosol scattering has been subtracted from each limb spectrum for convenience of comparison.

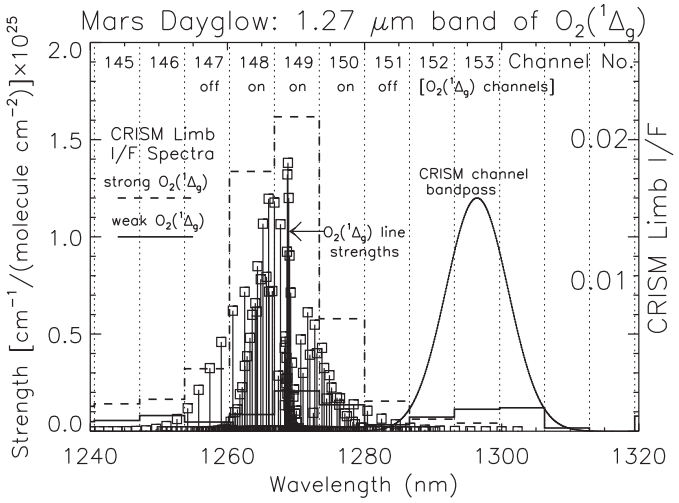

Fig. 1. CRISM limb spectra of $O_2(^1\Delta_g)$1.27 μm limb emission (L_s=152°, 22–25 km; solid histogram line-1S358W; dashed histogram line- 67N85W) in limb reflectance units (right vertical axis scale). are compared against a) the CRISM channel spacing/locations (dotted vertical lines), b) the CRISM instrumental resolution (solid Gaussian line at right, FWHM = 10.7 nm), and c) the location and relative strength of $O_2(^1\Delta_g)$ emission lines from 2008 HITRAN (vertical lines and box symbols, scale of left vertical axis). At the top of the figure, CRISM channel numbers and channel 'on','off' $O_2(^1\Delta_g)$assignments for RT/retrieval analysis are indicated.

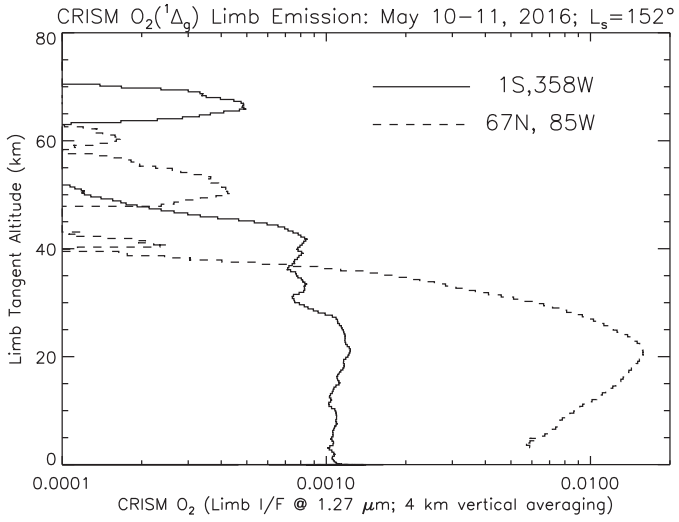

Fig. 2. CRISM limb profiles of $O_2(^1\Delta_g)$ emission, are presented in I/F reflectivity, for the same locations as spectra provided in Fig. 1 (L_s=152°). Here, limb profiles for $O_2(^1\Delta_g)$ emission are constructed as the difference between the average of the summed radiance in the three CRISM channels listed as 'on' in Fig. 1, and the average of the summed radiance in the two CRISM channels listed as 'off' in Fig. 1. $O_2(^1\Delta_g)$ emission is typically larger at high latitudes and decreases above 20–40 km altitudes, with peak layers often present above 50 km.

The RT retrieval analysis solves for both water ice and dust aerosol opacity profiles simultaneously with $O_2(^1\Delta_g)$ volume emission rates (VER), for self-consistent fits to the 'on-off' channel limb brightness differences as described below. Fig. 2 presents band integrated $O_2(^1\Delta_g)$ limb emission profiles for the CRISM limb spectra presented in Fig. 1, indicating the altitude dependences of these weak and strong cases for $O_2(^1\Delta_g)$ limb emission. Generally, the strongest observed $O_2(^1\Delta_g)$ emission occurs at lower altitudes and higher latitudes. However, the observed emission often decreases below 20 km altitudes due to collisional (pressure dependent) de-excitation and aerosol extinction along the limb path. Also generally, $O_2(^1\Delta_g)$ limb emission above 40–50 km altitudes falls below single limb measurement detection levels. However, distinct layers of $O_2(^1\Delta_g)$ emission are apparent at times, as indicated in Fig. 2. The 70 km emission layer presented in the low latitude Meridiani (1S,358W) limb emission profile of Fig. 2 coincides with mesospheric CO_2 clouds detected and well characterized in the full CRISM limb spectrum for this observation (not shown).

The limb $O_2(^1\Delta_g)$ emission presented in Figs. 1 and 2 is given in units of normal reflectance (I/F), through division by a solar flux spectrum. Atmospheric aerosol scattering leads to limb continuum reflectance levels approaching surface reflectances at altitudes below 10–30 km (depending on aerosol loading). For the purposes of Figs. 1 and 2, this scattering has been removed by simple subtraction of the average 'off' channel brightnesses in order to emphasize the signal level of the $O_2(^1\Delta_g)$ emission, which generally falls below 0.02 in I/F units over the CRISM channel average (Fig. 1). The spectral shape of this observed $O_2(^1\Delta_g)$ limb emission is closely matched by modeled $O_2(^1\Delta_g)$ emission employing the CRISM spectral bandpass, as demonstrated in polar night $O_2(^1\Delta_g)$ limb observations at altitudes above 40 km. In this case, lack of aerosol scattering or significant atmospheric extinction (gas and aerosol) allows extensive averaging of $O_2(^1\Delta_g)$ limb spectra for very high signal-to-noise ratio spectral shape comparisons (Clancy et al., 2012).

For the current topic of solar illuminated limb observations of $O_2(^1\Delta_g)$ dayglow throughout the atmosphere, careful treatment of aerosol extinction and scattering (and, to a lesser extent, CO_2 absorption) must be employed through spherical multiple scattering RT analysis. In the presentation of the RT and retrieval approaches, we begin with a brief description of the adopted $O_2(^1\Delta_g)$ molecular band parameters relevant to $O_2(^1\Delta_g)$ band emission calculations. Parameters associated with the comparison of $O_2(^1\Delta_g)$ emission and Mars O_3 and water vapor photochemistry (*i.e.*, LMDGCM simulations) are described briefly at the beginning of the model-data comparisons. These molecular and photochemical parameters for Mars $O_2(^1\Delta_g)$ analysis are more extensively detailed in previous publications (Novak et al., 2002; Krasnopolsky, 2003; Fedorova et al., 2006; Clancy et al., 2012; Guslyakova et al., 2014).

3. CRISM $O_2(^1\Delta_g)$ vertical profile retrievals

Vertical $O_2(^1\Delta_g)$ VER profiles are retrieved from CRISM limb spectra using two key elements, a pseudo-spherical limb RT code and a nonlinear profile retrieval algorithm. Both of these applications have been developed and applied to CRISM limb observations to retrieve dust/ice aerosol and H_2O abundance profiles in earlier studies (Smith et al., 2011, 2013). The addition of $O_2(^1\Delta_g)$ band emission is a new development, and so is presented below in some detail.

3.1. Retrieval approach

The retrieval of $O_2(^1\Delta_g)$ VER profiles follows a two-step process. Initially, the vertical profiles of dust and water ice aerosols are retrieved following the algorithm described in Smith et al. (2013). These aerosols define the continuum level against which the $O_2(^1\Delta_g)$ emission signal appears. The vertical distribution of aerosols further affects the detailed appearance of the $O_2(^1\Delta_g)$ signal through scattering and absorption of the $O_2(^1\Delta_g)$ band emission as viewed along the limb path. After the aerosol vertical profiles have been retrieved, RT modeling of the CRISM spectrum across the selected CRISM channels characterizing the $O_2(^1\Delta_g)$ emission (Fig. 1) is employed to retrieve the vertical distribution of $O_2(^1\Delta_g)$ volume emission rate (VER) in units of photons/cm^3/sec. Iteration between the aerosol and $O_2(^1\Delta_g)$ profile retrievals is not required as the aerosol retrieval employs CRISM spectral channels well separated from $O_2(^1\Delta_g)$ band emission.

The retrieval algorithm finds the $O_2(^1\triangle_g)$ vertical profile that provides the best fit, in a χ^2 sense, between the observed radiance (in the 5 CRISM channels indicated in Fig. 1, as a function of height above the surface) and the radiance computed from the forward RT model. The minimization is accomplished using the non-linear Levenberg-Marquardt retrieval algorithm presented in Press et al. (1992). The retrieved output quantity, the vertical profile of $O_2(^1\triangle_g)$ VER, is specified just above the surface and every 0.4 pressure scale heights between 0.2 and 9.4 scale heights above the surface. This typically gives coverage up to ~80 km above the surface with a vertical resolution of 3–4 km. The viewing geometry, including the incidence angle, emission angle, phase angle, and distance from Mars and the Sun, is provided by the MRO/CRISM project team.

3.2. Radiaive transfer (RT) approach

The forward RT model employs the discrete ordinates method to treat multiple scattering (Stamnes et al., 1988). The atmosphere is divided into vertical layers, and the number of radiation 'streams' is optimized to accurately model the angular distribution of the aerosol scattering. We use 50 atmospheric layers, each with a 0.2 scale height (~2 km) thickness, and 64 streams (32 pairs) to describe the radiation field. Atmospheric state variables, including aerosol and $O_2(^1\triangle_g)$ VER, are specified separately for each vertical layer. Aerosol particle sizes (effective radii, R_{eff}, of 1.5 μm for dust and 2.0 μm for ice) are adopted from RT modeling analyses of the spectral dependence of dust absorption in Mars Global Surveyor (MGS) Thermal Emission Spectrometer (TES) spectra (Wolff and Clancy, 2003) and multi-wavelength comparisons of TES, mini-TES (from the Mars Exploration Rovers), and CRISM spectra (Clancy et al., 2003; Wolff et al., 2006; 2009). Aerosol scattering properties are drawn from detailed RT modeling of CRISM emission phase function (EPF) spectra, which incorporate multiple emission angle measurements over a large set of locations and seasons to characterize surface and atmospheric (dust and ice) scattering phase functions (Wolff et al., 2009).

The limb geometry further requires that spherical geometry be explicitly treated in the RT modeling. We adopt a 'pseudo-spherical approximation' to full spherical RT (Spurr, 2002; Thomas and Stamnes, 2002; Smith et al., 2013), in which the diffuse radiation field is calculated via plane-parallel discrete ordinates RT. The vertically dependent source functions derived from this plane parallel RT field are integrated along spherical limb paths appropriate to CRISM limb observations. These pseudo-spherical RT calculations are at least two orders of magnitude faster than an 'exact' Monte Carlo approach (Whitney et al., 1999; Wolff et al., 2006), while providing accuracies of order a few percent over a wide range of Mars scattering conditions (Smith et al., 2013).

3.3. $O_2(^1\triangle_g)$ emission added to RT

The RT code used in this analysis is identical to that employed by Smith et al. (2013) except for the addition of $O_2(^1\triangle_g)$ volume emission to the source function, and the inclusion of weak CO_2 band absorption affecting the lower two wavelength channels of modeled $O_2(^1\triangle_g)$ emission (1.255–1.268 μm, see Fig. 3 of Fedorova et al. (2006)). This CO_2 gas absorption is included via the correlated-k approximation with HITRAN 2004 line strength parameters (Rothman et al., 2005). The wavelength dependence of $O_2(^1\triangle_g)$ volume emission is treated line-by-line, based on HITRANS 2008 line strength parameters (Rothman et al., 2009), and convolved to CRISM spectral channel resolution prior to RT modeling. Inclusion of $O_2(^1\triangle_g)$ spectral line emission in the correlated-k quadrature scheme is unnecessary because the total CO_2 absorption is small and there is negligible overlap of the $O_2(^1\triangle_g)$ emission with CO_2 absorption bands at line-by-line resolution.

$O_2(^1\triangle_g)$ emission has distinct functional dependences from thermal emission, such that it is explicitly inserted in the internal source function of the existing pseudo-spherical RT code. Consequently, the RT internal source function $Q_\lambda(\tau, \mu, \phi)$ [as defined in Thomas and Stamnes (2002)], is modified as:

$$Q_\lambda(\tau,\mu,\phi) = \frac{\sigma_\lambda}{d\tau/dz(\tau)} + (1-\omega_\lambda(\tau))B_\lambda(\tau) + Q_\lambda^{solar}(\tau,\mu,\phi) \quad (1)$$

The effective vertical coordinate τ is the total (aerosol and CO_2) optical depth, ϕ is the solar azimuth angle, and μ is the cosine of the zenith angle. The second term on the right side of Eq. (1) represents the contribution of thermal emission, where $\omega_\lambda(\tau)$ is the weighted (aerosol and CO_2) single scattering albedo and B_λ is the Planck function. Although included in the RT analysis of $O_2(^1\triangle_g)$ emission, thermal emission is negligible except over the 3.3-3.7 μm wavelength range regarding the separate aerosol opacity retrievals (Smith et al., 2013). The third term of Eq. (1) represents the contribution of the solar beam, $Q_\lambda^{solar}(\tau,\mu,\phi)$, to the source function, where the solar spectrum is adopted from the MODTRAN atmospheric radiation code (Berk et al., 1998).

The first term of Eq. (1) represents the added $O_2(^1\triangle_g)$ contribution to the internal source function $Q_\lambda(\tau, \mu, \phi)$. Here, σ_λ is the specific volume emission rate (calculated by multiplying the $O_2(^1\triangle_g)$ VER by its normalized wavelength dependence, such that that its wavelength dependence sums to unity over the band). In this case, the $O_2(^1\triangle_g)$ contribution to radiance per unit distance l is:

$$\frac{dI_\lambda^{O2del}}{dl} = \sigma_\lambda(\tau) \quad (2)$$

With altitude denoted by z and the extinction coefficient by β, $O_2(^1\triangle_g)$ is expressed in the vertical τ coordinate as:

$$\frac{dI_\lambda^{O2del}}{d\tau} = \sigma_\lambda(\tau)\frac{dl}{d\tau} = \sigma_\lambda(\tau)\beta_\lambda(\tau) = \frac{\sigma_\lambda(\tau)}{d\tau/dz(\tau)} \quad (3)$$

A technical consequence of inserting into the RT code an emission source not intrinsically dependent on τ is that numerical instability can occur over conditions of near-zero $d\tau/dz$. To counteract this instability, each model RT layer is specified to contain non-zero values for optical depth. More specifically, a minimum level optical depth in the form of a gas absorber (ω_λ=0) is set for all vertical layers in the RT calculations. The value of this minimum τ is vanishingly small in terms of measureable impact on retrieved $O_2(^1\triangle_g)$ VER (or separately modeled aerosol values).

3.4. $O_2(^1\triangle_g)$ profile retrieval characteristics

The sensitivity, vertical extent, and error limits of CRISM $O_2(^1\triangle_g)$ VER profile retrievals are demonstrated in Fig. 3, which presents a subset of retrievals (out of ~1100) for a broad range of latitudes, longitudes, and seasons (L_s). CRISM observed $O_2(^1\triangle_g)$ VER are presented in units of 10^6 photons/cm^3/second (as are subsequently presented LMDGCM model VER). These units are equivalent to 100 kR/km, in the kilo-Rayleigh/km VER units presented in previous $O_2(^1\triangle_g)$ polar nightglow (Bertaux et al., 2012; Clancy et al., 2012; 2013b) and dayglow (Guslyakova et al., 2014; 2016) studies. A limb brightness of roughly 50 MRay (Mega-Rayleighs) corresponds to a VER of 10^6 photons/cm^3/second (assuming no aerosol extinction and Mars atmospheric limb geometry) .

The baseline retrieval files are provided on fixed pressure coordinate intervals such that, as the Mars atmospheric temperature (*i.e.*, scale height) decreases with altitude, the vertical resolution in km decreases with altitude. In addition, the surface altitude/pressure also varies spatially (and seasonally, to a lesser

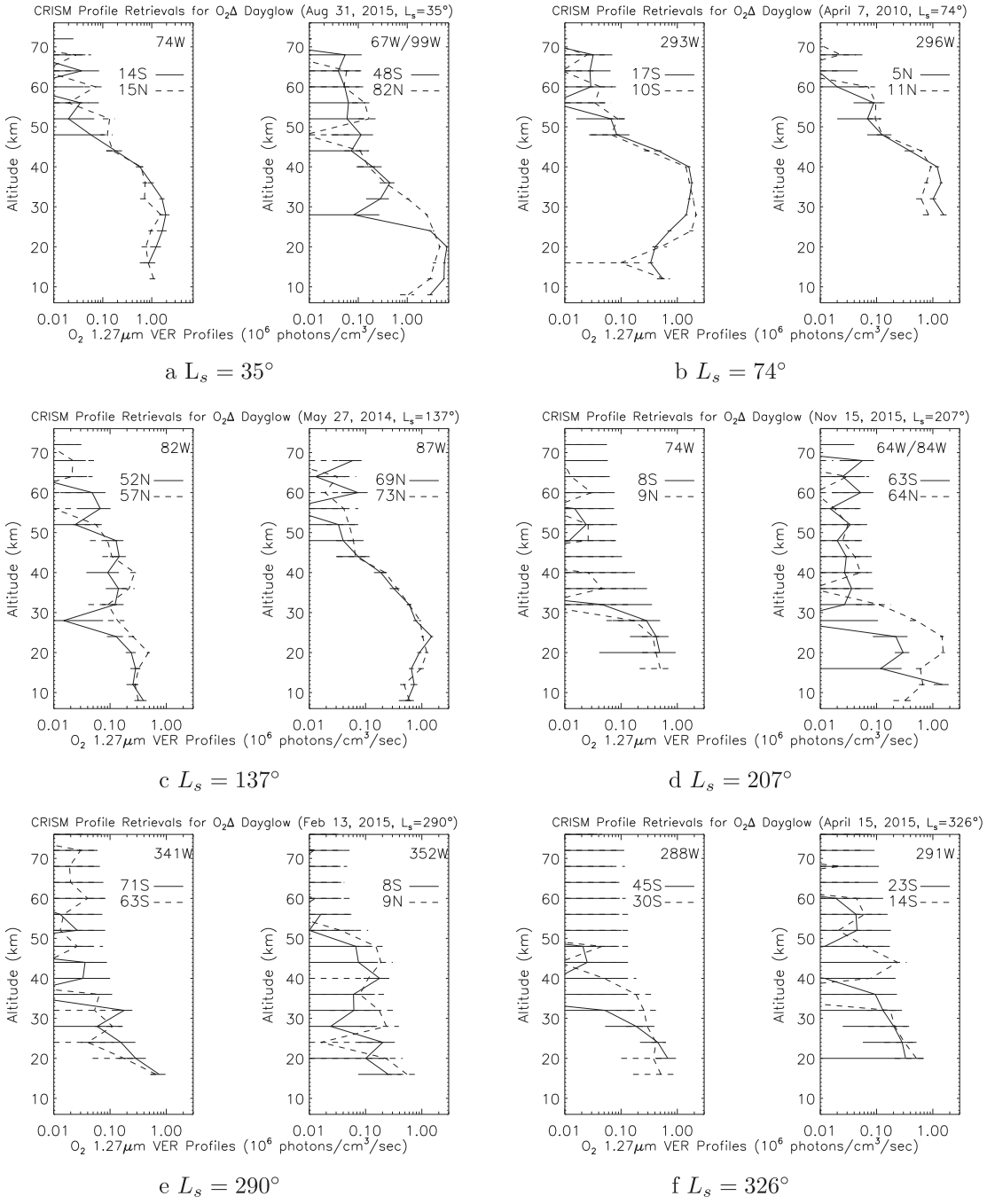

a $L_s = 35°$ b $L_s = 74°$

c $L_s = 137°$ d $L_s = 207°$

e $L_s = 290°$ f $L_s = 326°$

Fig. 3. A set of CRISM $O_2(^1\triangle_g)$ volume emission rate (VER) retrieved profiles is displayed for a range of seasons (L_s) and locations (two latitudes per figure, at a given longitude). The presented 1-σ error bars represent measurement errors associated with measurement noise and the Levenberg–Marquardt retrieval algorithm.

degree) on Mars. Hence, the specific altitude levels among the $O_2(^1\triangle_g)$ profile retrievals are variable. For the purposes of this presentation, the full set of $O_2(^1\triangle_g)$ profile retrievals are interpolated to a standard aeroid altitude scale with a fixed 4 km grid spacing from 4 to 76 km. This same procedure is applied to LMDGCM $O_2(^1\triangle_g)$ profile comparisons, which are selected for comparable locations (latitude, longitude), seasons (L_s), and local times (LT) to each 4 km gridded $O_2(^1\triangle_g)$ profile retrieval (as discussed in following sections).

3.5. Retrieval vertical extent

The retrieval vertical extent for this gridded profile data set always extends to 76 km, although measurable $O_2(^1\triangle_g)$ signal is rarely present above 60 km altitudes. The lower boundary of retrieval is generally above 8 km, commonly above 16 km, and occasionally above 28 km. This variable lower altitude limit reflects variable aerosol (dust and ice) loading in the Mars atmosphere versus space and time, which sets a minimum limb transmission beyond which limb tangent altitude $O_2(^1\triangle_g)$ emission cannot be retrieved. Although dust opacity typically exceeds ice optical depths in the Mars atmosphere, the aphelion cloud belt (e.g., 5–11N in Fig. 3b, as also evident in the left panel of Fig. 9) and polar hood ice aerosols more commonly limit vertical extents for $O_2(^1\triangle_g)$ retrievals. This is because ice aerosols are typically concentrated at higher altitude levels (e.g., 15–35 km), whereas dust is more generally confined near the surface, at least under well mixed conditions. It is also true that the 2009–2016 (primarily MY30-33) range

of CRISM limb observations does not include planet encircling (vertically extended) dust storm conditions.

3.6. Sensitivity limits

The inherent sensitivity limits of CRISM $O_2(^1\triangle_g)$ profile retrievals are also demonstrated in Fig. 3. For low aerosol scattering conditions (e.g., Fig. 3c), $O_2(^1\triangle_g)$ values of 0.05×10^6photons/cm^3/sec (5 kR/km) can be retrieved at the one-sigma level in a single profile retrieval. However, the sensitivity of CRISM VER profile retrievals is also affected by variable aerosol scattering/extinction along the limb viewing path, which limits limb path transmission and increases channel-to-channel noise due to the increased spectral background brightness. This behavior is apparent during the dusty perihelion atmospheric conditions represented in Fig. 3e and f. The 1σ error bars presented in Fig. 3 are returned from the Levenberg-Marquardt retrieval algorithm, reflecting measurement noise in the context of the vertical profile inversion, including aerosol extinction/scattering effects.

3.7. The extended set of CRISM $O_2(^1\triangle_g)$ profile retrievals

The full set of CRISM $O_2(^1\triangle_g)$ profile retrievals is provided in Fig. 4, which presents the latitude/L_s behaviors for $O_2(^1\triangle_g)$ VER at 6 aeroid altitude levels of 12, 20, 28, 36, 44, and 52 km. Although additional 4-km grid levels exist over 8–80 km, Fig. 4 exhibits the key characteristics of Mars atmospheric $O_2(^1\triangle_g)$ dayglow emission. These include large spatial/temporal variability, high latitude enhancements, strong orbital (L_s) variability, peak emission over 8–44 km altitudes, and weaker variable emission at 48–60 km altitudes. The large L_s variation at higher altitude levels (28–44 km versus 12 and 20 km) reflects the strong orbital dependence in the Mars atmospheric water vapor saturation conditions. As described subsequently, the lower altitude level measurements provide specific sensitivity to the collisional de-excitation of $O_2(^1\triangle_g)$, and all altitude levels are sensitive to atmospheric water vapor abundance.

Fig. 4 also illustrates the uneven measurement coverage in L_s, with much reduced coverage over the perihelion (L_s = 180–360°) to early northern spring (L_s = 30°) periods. This L_s coverage bias is largely circumstantial, but it is also true that higher dust loading and reduced $O_2(^1\triangle_g)$ VER limit detection capability. Only $\geq 1\sigma$ detection measurements are represented in these plots.

4. LMDGCM simulations of $O_2(^1\triangle_g)$ VER profiles

Interpretation of Mars $O_2(^1\triangle_g)$ VER profiles is complex in at least two aspects, the need to employ a Mars GCM photochemical model and the need to employ considerable temporal/spatial averaging in such model-data comparisons. The latter limitation reflects the extreme variability of Mars $O_2(^1\triangle_g)$ emission as forced by similarly extreme Mars atmospheric water vapor variability, particularly with respect to vertical profile comparisons (Maltagliati et al., 2013). The former limitation follows from the derivative nature of $O_2(^1\triangle_g)$ emission, which depends on solar illumination-dependent O_3 photolysis rates (*i.e.*, photometric angles and atmospheric extinction), on atmospheric density-dependent molecular properties (*eg*, collisional de-excitation by CO_2), and most significantly on Mars O_3 photochemistry. Mars O_3 photochemistry depends on a number of atmospheric parameters, the most important of which is water vapor. Mars water vapor, in turn, is dependent on non-local surface sources (e.g., polar ice reservoirs), global transport (horizontal and vertical), and highly temperature-sensitive vapor saturation conditions (including cloud microphysics). Hence, a sophisticated MGCM capable of simulating O_3 photochemistry and the complete spatial distribution of water vapor as a function of time (LT and L_s) and space (latitude, longitude, altitude) is a necessary requirement for quantitative interpretation of the CRISM $O_2(^1\triangle_g)$ profile data set. In fact, implications regarding the spatial/seasonal distribution of Mars water vapor constitute a major focus for the $O_2(^1\triangle_g)$ model-data comparisons of this study.

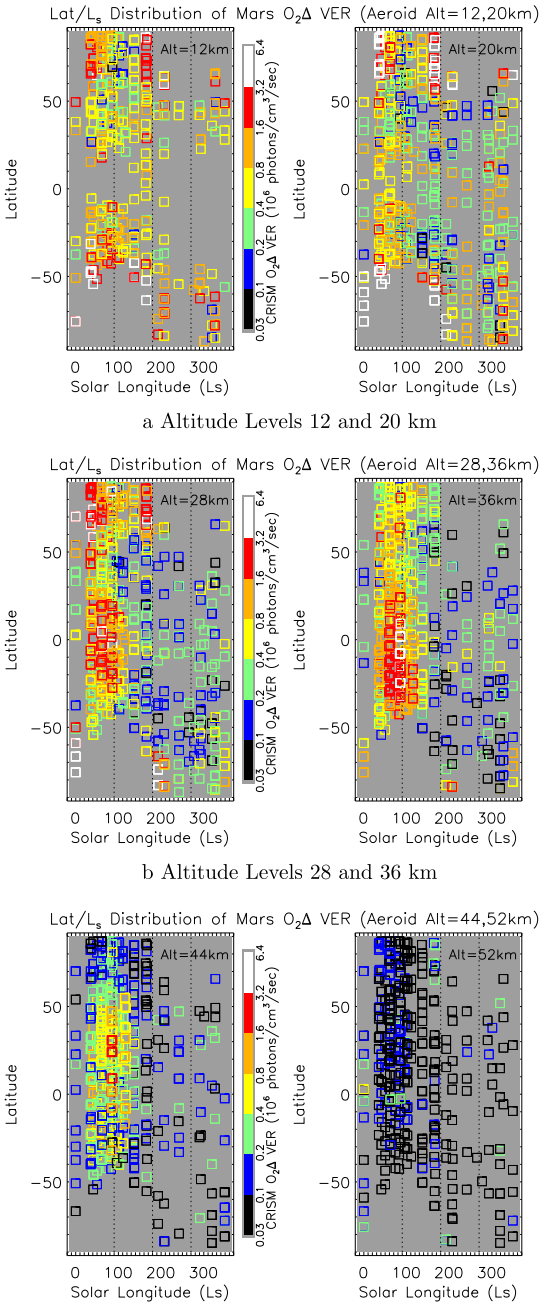

a Altitude Levels 12 and 20 km

b Altitude Levels 28 and 36 km

c Altitude Levels 44 and 52 km

Fig. 4. The latitudinal/seasonal (L_s) distributions of CRISM retrieved $O_2(^1\triangle_g)$ volume emission rates (VER, in 10^6 photons/cm^3/sec) are presented for gridded aeroid altitude levels of a) 12 and 20 km, b) 28 and 36 km, and c) 44 and 52 km. The $O_2(^1\triangle_g)$ VER are presented in binned color ranges according to the provided color scale bars. Vertical dotted lines indicate L_s values of 90°, 180°, and 270°.

There are a number of Mars GCM codes adapted for photochemical simulations, particularly for O_3, which constitutes the most extensive Mars photochemical database (Lefèvre et al., 2004; Moudden and McConnell, 2007; Neary and Daerden, 2013). The Laboratoire de Météorologie Dynamique (LMD) GCM is the most

extensively developed such code, in terms of range of modeled species and published comparisons to extensive observational data sets. LMDGCM studies have been conducted for Mars O_3 (Lefèvre et al., 2004; Perrier et al., 2006; Lebonnois et al., 2006; Lefèvre et al., 2008; Montmessin and Lefèvre, 2013; Clancy et al., 2016), H_2O_2 (Encrenaz et al., 2008; 2015), $O_2(^1\triangle_g)$ (Bertaux et al., 2012; Gagné et al., 2012; Clancy et al., 2012; 2013a; Guslyakova et al., 2016), CH_4 (Lefèvre and Forget, 2009), OH (Clancy et al., 2013a), NO (Gagné et al., 2013), CO (Encrenaz et al., 2006; Clancy et al., 2016), and thermospheric/ionospheric chemistry (González-Galindo et al., 2013; Chaufray et al., 2015). Of particular value to the current study, the LMDGCM has been employed widely in interpretation of water vapor measurements, including the affects of cloud microphysics, cloud radiative heating, and supersaturation conditions (Montmessin et al., 2004; Madeleine et al., 2012; Maltagliati et al., 2013; Navarro et al., 2014).

4.1. LMDGCM simulations of $O_2(^1\triangle_g)$ and H_2O

The presented LMDGCM simulations employ the latest LMDGCM photochemical configuration, including a detailed cloud microphysical scheme that provides for dust particle scavenging, water vapor supersaturation, and variable particle size effects. Navarro et al. (2014) shows that treatment of these processes significantly improves model-data agreement for the seasonal/latitudinal distribution of Mars atmospheric water columns, which had deteriorated with the inclusion of cloud radiative forcing in earlier LMDGCM simulations (Haberle et al., 2011; Madeleine et al., 2012; Urata and Toon, 2013). These changes in the LMDGCM treatment of cloud microphysics, including dust interactions, also lead to significant changes in modeled water vapor vertical profiles, through vertical redistribution associated with water ice gravitational settling and through water vapor supersaturation associated with cloud nucleation limitations (Navarro et al., 2014). However, the modeled vertical distributions of water vapor are less constrained by reasonably well observed water vertical columns (e.g.; Smith, 2004; Fedorova et al., 2006; Fouchet et al., 2007; Smith et al., 2009; Trokhimovskiy et al., 2015), which are dominated by lower ($z\leq$ 10-15 km) atmospheric water.

Water vapor profile comparisons between LMDGCM simulations and observations are hampered by the lack of H_2O profile retrievals with sufficient seasonal/latitudinal coverages. This is a significant limitation given the relevance of such profiles on Mars atmospheric water transport, clouds, and photochemistry. SPICAM solar occultation measurements indicate both the potential importance of supersaturation and the extreme variability of water vapor above 20–30 km altitudes (Maltagliati et al., 2011; 2013). Navarro et al. (2014) demonstrate that SPICAM solar occultation profile retrievals for water vapor are generally supportive of current LMDGCM simulated supersaturation conditions. However, SPICAM water vapor profile retrievals are limited in seasonal/latitudinal coverage. This, coupled with the extreme spatial/temporal variability of water vapor profiles, limits model-data comparisons of global water vapor profile behaviors.

Although not a direct measurement of water vapor, CRISM $O_2(^1\triangle_g)$ profiles bring several new advantages to observationally constraining Mars atmospheric water vapor profiles. As shown in Fig. 5, LMDGCM water vapor and $O_2(^1\triangle_g)$ VER are anti-correlated over 2–3 orders of magnitude variations due to very direct photochemical coupling between these species in the Mars atmosphere (see also, Fig. 8 of Guslyakova et al., 2016). The full latitude/season (CRISM corresponding) set of LDMGCM $O_2(^1\triangle_g)$, H_2O values at 24 km aeroid altitude is presented in the left panel against a simple inverse dependence (dashed line). The right panel defines this inverse relationship with reduced scatter for a more restricted seasonal/spatial regime (corresponding to the aphelion cloud belt), where the variations of other factors (atmospheric density, O_3 and H_2O photolysis rate coefficients, etc.) are minimized.

This supports a fairly direct inference of water vapor profiles from $O_2(^1\triangle_g)$ profiles based on LMDGCM photochemical simulations. Secondly, the extensive seasonal and latitudinal coverage and number of the CRISM $O_2(^1\triangle_g)$ profile retrievals (Table 1) supports definitions of seasonal/latitudinal average behaviors, which in turn constrains seasonal/latitudinal averages for water vapor profile distributions. Furthermore, the anti-correlation of water vapor and $O_2(^1\triangle_g)$ emission means that CRISM sensitivity is optimized for low rather than high water vapor abundances, which is opposite that for direct water vapor measurements, such as by SPICAM solar occultation measurements. Consequently, although CRISM $O_2(^1\triangle_g)$ profile retrievals are not a direct water vapor measurement, they actually provide significant new constraints on the Mars atmospheric water vapor distribution versus altitude, season (L_s), and latitude.

4.2. LMDGCM simulation cases

The presented LMDGCM simulations are characterized by the same longitude/latitude grid spacing (64×48) as in Navarro et al. (2014), but with a more extensive altitude range (~150 km vs 80–100 km) to facilitate ongoing $O_2(^1\triangle_g)$ comparisons over 60–100 km altitudes. Model radiative and photochemical parameters and processes are described in prior observational comparisons with the LMDGCM (e.g. Lefèvre et al., 2004; Perrier et al., 2006; Lebonnois et al., 2006; Lefèvre et al., 2008; Madeleine et al., 2012; Bertaux et al., 2012; Clancy et al., 2012; Guslyakova et al., 2016; Clancy et al., 2016). These include heterogeneous chemistry, cloud radiative forcing, interactive dust, and cloud microphysical approaches developed by Lefèvre et al. (2008), Madeleine et al. (2012), and Navarro et al. (2014). In the interactive dust scheme, dust columns are fixed to the Mars Climate Sounder MY26 climatology from Montabone et al. (2014) and the vertical profile of dust abundance is adjusted according to calculated effects of global transport, gravitational settling, and dust scavenging by ice clouds.

Aside from the significant modifications in water vapor profile calculations introduced by Navarro et al. (2014), the LMDGCM $O_2(^1\triangle_g)$ photochemical and molecular properties are the same as employed for Mars polar $O_2(^1\triangle_g)$ nightglow studies (Bertaux et al., 2012; Clancy et al., 2012). However, a key distinction in $O_2(^1\triangle_g)$ dayglow analysis is the dominance of the ozone photolysis contribution,

$$O_3 + h\nu \rightarrow O_2(^1\triangle_g) + O \quad (4)$$

over termolecular recombination of atomic oxygen

$$O + O + CO_2 \rightarrow O_2(^1\triangle_g) + CO_2 \quad (5)$$

for Mars $O_2(^1\triangle_g)$ dayglow. Both of these modeled contributions are added in comparisons to CRISM $O_2(^1\triangle_g)$ dayglow observations, but the contribution from O_3 photolysis dominates to altitudes above 60 km. Hence, Mars $O_2(^1\triangle_g)$ dayglow is predominately dependent on Mars water vapor (rather than atomic oxygen density) over the full altitude range of the presented CRISM $O_2(^1\triangle_g)$ retrievals.

Apart from the detailed distribution of Mars atmospheric water vapor, two additional atmospheric processes affecting Mars $O_2(^1\triangle_g)$ dayglow are currently uncertain. The first process regards heterogeneous (ice cloud) removal of atmospheric HO_2 and OH, photolysis products of water vapor that catalytically reduce O_3 and hence $O_2(^1\triangle_g)$ emission (Lefèvre et al., 2008). The efficiency of this process remains uncertain (Clancy et al., 2016), but its inclusion in LMDGCM photochemical simulations can improve model-data comparisons for high latitude column O_3 measurements (Lefèvre et al., 2008; Clancy et al., 2016). Given that $O_2(^1\triangle_g)$ originates from

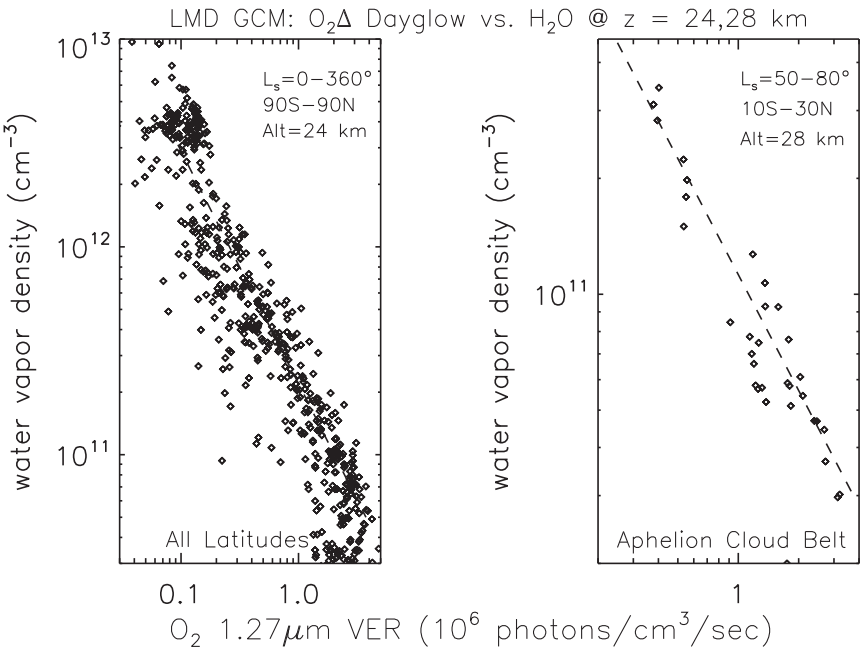

Fig. 5. The LMDGCM simulated values for $O_2(^1\Delta_g)$ VER and water vapor density are plotted against one another for all locations/times of CRISM $O_2(^1\Delta_g)1\sigma$ detection measurements at an aeroid altitude of 24 km, and more narrowly within the aphelion cloud belt (ACB, right panel) for an aeroid altitude of 28 km. Dashed lines indicate simple inverse proportional dependences, where a single such line reasonably fits a much narrower range of other model parameter variations (such as photolysis rate coefficients) for the ACB region (right panel). Model water vapor abundance and $O_2(^1\Delta_g)$ emission exhibit inverse proportionality over ~ 2 orders-of-magnitude variation.

O_3 photolysis, it is useful to compare model-observed $O_2(^1\Delta_g)$ profiles for simulations with and without heterogeneous chemistry on Mars water ice clouds. This provides some indication of the degree to which current photochemical modeling uncertainties impact comparisons between LMD GCM simulated and CRISM retrieved $O_2(^1\Delta_g)$ VER profiles. As it turns out, the modeled $O_2(^1\Delta_g)$ sensitivity to this effect is concentrated to higher latitudes and lower altitudes where the second key modeling uncertainty also becomes most influential. This second parameter regards the de-excitation of $O_2(^1\Delta_g)$ through CO_2 collisions, which is also a measurement target for the current analysis.

The timescale for collisional de-excitation of the electronically excited $O_2(^1\Delta_g)$state approaches its radiative timescale for 1.27 μm emission (4460 s; Lafferty et al., 1998) at lower atmospheric, peak CO_2 densities. As a consequence, CO_2 collisional de-excitation plays a significant role in reducing $O_2(^1\Delta_g)$ emission, particularly below 20 km altitudes. Currently, the rate coefficient for $O_2(^1\Delta_g)$ collisional de-excitation by CO_2, K_{CO2}, is poorly known from laboratory constraints (Leiss et al., 1978; Burkholder et al., 2015) and so has been the subject of several analyses associated with Mars column $O_2(^1\Delta_g)$ observations (Krasnopolsky, 2009; Gagné et al., 2013; Guslyakova et al., 2016). The current set of CRISM $O_2(^1\Delta_g)$ VER profile retrievals is better suited to this task as lower atmospheric $O_2(^1\Delta_g)$ VER, which are disproportionately dependent on CO_2 collisional de-excitation, can be assessed separately from $O_2(^1\Delta_g)$ above 20 km altitudes. Consequently, CRISM $O_2(^1\Delta_g)$ VER below 20 km altitude are employed to constrain K_{CO2}. Because such $O_2(^1\Delta_g)$ (or O_3) also depends on the model water vapor below 20 km altitudes, the derived $K_{CO2}$is correlated with the global/seasonal average for model water abundances below 20 km altitudes, or effectively with observed average atmospheric water columns for which the model has been tuned to simulate. However, this error source is considerably smaller than contributed by the uncertain effects of heterogeneous chemistry, as treated below.

Towards the derivation of K_{CO2}, LMDGCM $O_2(^1\Delta_g)$ comparison values are calculated for K_{CO2}= 0.73, 0.50, 0.25, and 0.125×10^{-20} cm^3sec^{-1}. This range includes recently derived estimates (e.g. Guslyakova et al., 2016) and encompasses the current estimated value. Model $O_2(^1\Delta_g)$ VER are calculated offline from the stored output of LMDGCM simulations, as $O_2(^1\Delta_g)$ is a simple product (rather than active participant) of Mars photochemistry. This variation in $K_{CO2}$is calculated from full LMDGCM simulations with and without heterogeneous chemistry, which forces additional variations in primarily high latitude $O_2(^1\Delta_g)$) (or O_3) independent of water vapor abundance.

Additional LMDGCM simulations, in which the LMDGCM water vapor distribution is modified to bring about improved model-data agreement for $O_2(^1\Delta_g)$ VER profiles, are not attempted. This would require detailed analysis of the complex set of LMDGCM model parameters that are currently tuned to achieve model-data agreement in the global/seasonal distribution of Mars atmospheric water vapor columns (Navarro et al., 2014). It is not clear how simply these same model parameters may be adjusted to affect specific water vapor profile changes, nor how well available water vapor profile and $O_2(^1\Delta_g)$ observations would guide such tuning. Instead, model-data comparisons for $O_2(^1\Delta_g)$ VER profiles versus latitude and season (L_s) are characterized in terms of derived global water vapor profile differences relative to the current Navarro et al. (2014) standard. The spatial/seasonal character of these differences are then discussed in terms of atmospheric processes that affect Mars water vapor profiles, such as transport and cloud microphysics, in the context of the Navarro et al. (2014) analysis.

5. Model-data comparisons for $O_2(^1\Delta_g)$ VER profiles

Extreme (order-of-magnitude) local variability in both LMDGCM simulated and CRISM retrieved $O_2(^1\Delta_g)$ VER results from extreme temperature sensitivity to water vapor saturation conditions (e.g., Fig. 5). Fig. 6 indicates model-data correspondence within the aphelion cloud belt. Each plotted point indicates model (ordinate) and data (abscissa) values for colocated (latitude,longitude,altitude), cotemporal (L_s, LT) comparison points over L_s=60–100°, 20S–30N latitudes, and 24–32 km aeroid altitudes. Absence of detailed correlation between modeled (LMDGCM) and

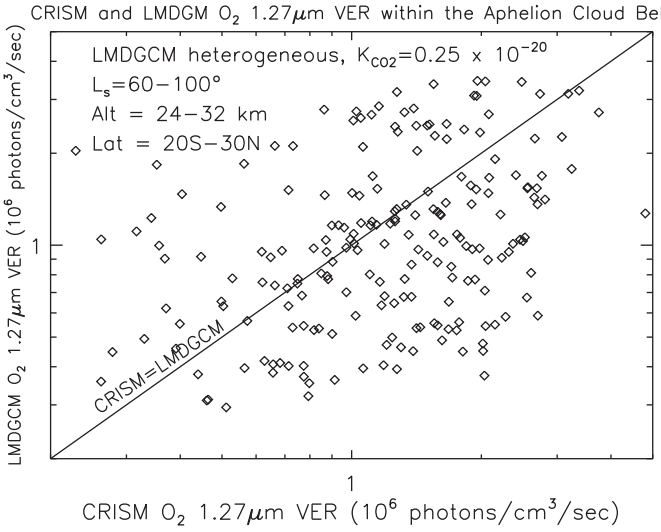

Fig. 6. The correspondence of co-located, co-temporal LMDGCM (vertical axis) and CRISM retrieved (horizontal axis) $O_2(^1\triangle_g)$ VER within the aphelion cloud belt region (L_s=60−100°, 20S–30N, 24–32 km aeroid altitudes). One-to-one correspondence is weak due to lack of detailed correspondence between LMDGCM modeled and CRISM observed local temperature/water abundance conditions. The apparent average correlation (solid line) reflects average model-data L_s/latitude/altitude trends in water vapor, and hence $O_2(^1\triangle_g)$ emission, over the binned region/period.

actual (CRISM) atmospheric temperature variability at a given location and time masks global and seasonal correlations between model and observed $O_2(^1\triangle_g)$ VER. Fig. 6 clearly exhibits an average correlation between CRISM and LMDGCM $O_2(^1\triangle_g)$ VER distributions associated with average latitudinal, altitude, and L_s trends within the presented aphelion cloud belt (ACB) extents. But Fig. 6 also demonstrates that considerable spatial/temporal binning is required to map such large-scale correspondences between model and observed $O_2(^1\triangle_g)$ VER distributions.

Fig. 6 model results employ heterogeneous chemistry and an $O_2(^1\triangle_g)$ collisional de-excitation rate coefficient (K_{CO2}) of 0.25×10^{-20} cm^3sec^{-1}. All of the following model-data comparisons adopt this baseline LMDGCM configuration, with the exception of model-data comparisons applied to a best-fit determination for K_{CO2}. This reflects the resulting best-fit value for K_{CO2}so obtained and the currently standard heterogeneous chemistry mode for LMDGCM photochemical simulations (Lefèvre et al., 2015b).Figs. 7 and 8 compare model and observed $O_2(^1\triangle_g)$ VER versus L_s for low latitudes and northern high latitudes, respectively. The two presented panels in Fig. 7 for low latitudes (30S–30N) demonstrate relatively modest (surface) longitudinal variations for $O_2(^1\triangle_g)$ VER at 28–32 km altitudes, as exhibited over Valles/Meridiani (left panel) versus Hellas Basin (right panel) longitudes. Fig. 7 does suggest that observed $O_2(^1\triangle_g)$ emission extends longer over the aphelion, northern summer season (L_s=100–140°) for the Valles/Meridiani versus Hellas longitude corridor, which is less evident in the model $O_2(^1\triangle_g)$ VER. Furthermore, observed (CRISM) low latitude $O_2(^1\triangle_g)$ over the perihelion, southern summer season (L_s=140–330°) reaches minimum values 2–3 times larger than exhibited by the model (LMDGCM). This behavior is also exhibited in Mars O_3 column measurements (Lefèvre et al., 2015b), which suggests that model water vapor abundances above 20 km altitudes are too large for the perihelion half of the Mars year at low latitudes. This behavior is explored over a larger range of latitudes and altitudes in following figures presented in this paper.

Fig. 8 presents northern high latitude $O_2(^1\triangle_g)$ VER over 20–24 km altitudes, for latitude ranges of 50–60N (left panel) and 60–70N (right panel). Peak $O_2(^1\triangle_g)$ VER in northern spring/early summer (L_s=40–70°), early fall (L_s=140–200°), and late winter (L_s=330–360°) exhibit general agreement between observed and modeled $O_2(^1\triangle_g)$ VER. However, CRISM $O_2(^1\triangle_g)$ VER fall below LMDGCM values by as much as an order-of-magnitude around northern summer solstice (L_s=70–130°). This behavior is less apparent in observations of Mars O_3 column abundances (Clancy et al., 2016), suggesting enhanced vertical extension of high latitude water vapor for observed versus modeled conditions.

5.1. Latitude/altitude cross-sections for $O_2(^1\triangle_g)$ VER

To better explore such latitudinal and vertical distinctions between CRISM and LMDGCM $O_2(^1\triangle_g)$, a set of latitude/altitude plots for CRISM/LMDGCM $O_2(^1\triangle_g)$ VER ratios are presented in Figs. 9 and 10 for L_s bins of 30–60°, 60–140°, 200–310°, and 320–360°. These L_s bins are selected to represent Mars atmospheric seasonal/orbital variations, but are also constrained by the uneven L_s coverage obtained for CRISM limb observations (Fig. 4). Here, again, the model values correspond to the case of heterogeneous chemistry and a value of 0.25×10^{-20} cm^3sec^{-1} for K_{CO2}. Both of these model parameters are most important for simulated $O_2(^1\triangle_g)$ VER at altitudes below 20 km, and are explicitly addressed in the following section.

The northern spring/summer (aphelion) periods presented in Fig. 9 indicate several key areas of disagreement between model and observed $O_2(^1\triangle_g)$ VER. CRISM observed $O_2(^1\triangle_g)$ above ~40 km are 2–3 times larger than LMDGCM model values for both L_s periods, a behavior which also extends to the southern summer/perihelion periods of Fig. 10. In contrast, CRISM observed $O_2(^1\triangle_g)$ over ~15 to 35 km altitudes are 2–5 times smaller LMDGCM model values. This behavior extends over 40S to 60N latitudes for the northern spring L_s=30–60° period (left panel), but is confined to 30–90N latitude in the northern summer L_s=60–140° period (right panel). This behavior at northern mid-to-high latitudes corresponds, in latitude and L_s, to a distinct minimum in observed O_3 column densities (Perrier et al., 2006; Clancy et al., 2016) and cloud optical depths (Clancy et al., 1999; Wolff et al., 2010), indicating elevated water vapor abundances yet minimal lower level (*i.e.*, column integrated) cloud optical opacities between the aphelion cloud belt (ACB) and the spring/summer north polar atmosphere. This behavior apparently extends to southern mid-latitudes over L_s=30–60° (left panel), before the formation of the ACB.

Fig. 10 presents latitude/altitude distributions of the ratio for $O_2(^1\triangle_g)$ VER, CRISM/LMDGCM, during southern summer (left panel, L_s=200–310°) and fall (right panel, L_s=320–360°) periods. $O_2(^1\triangle_g)$ ratios for these periods are less well sampled and so present greater scatter (noise) and missing values (at least 4 measurements are required for a bin to be represented in these figures). Nevertheless, patterns in the CRISM/LMDGCM $O_2(^1\triangle_g)$ ratios indicate several general trends. Foremost of these is generally larger observed versus modeled $O_2(^1\triangle_g)$ emission. Similar to the L_s comparisons of Fig. 9, 2-3 times larger observed $O_2(^1\triangle_g)$ emission is present above 30–40 km altitudes over most latitudes, peaking at high northern latitudes. Particularly striking is the very large observed $O_2(^1\triangle_g)$ emission over 10–30 km altitudes above the southern summer polar region (left panel, 3–6 times model values). A fraction of this effect is due to the fact that the Navarro et al. (2014) LMDGCM configuration overestimates water columns in this region by ~50% relative to water column measurements (Smith, 2004; Trokhimovskiy et al., 2015). The much larger observed increases in $O_2(^1\triangle_g)$ VER relative to the model suggest that water vapor released from the southern summer polar cap is more effectively confined to lower altitudes than simulated by the model. In fact, Navarro et al. (2014) did not tune southern polar

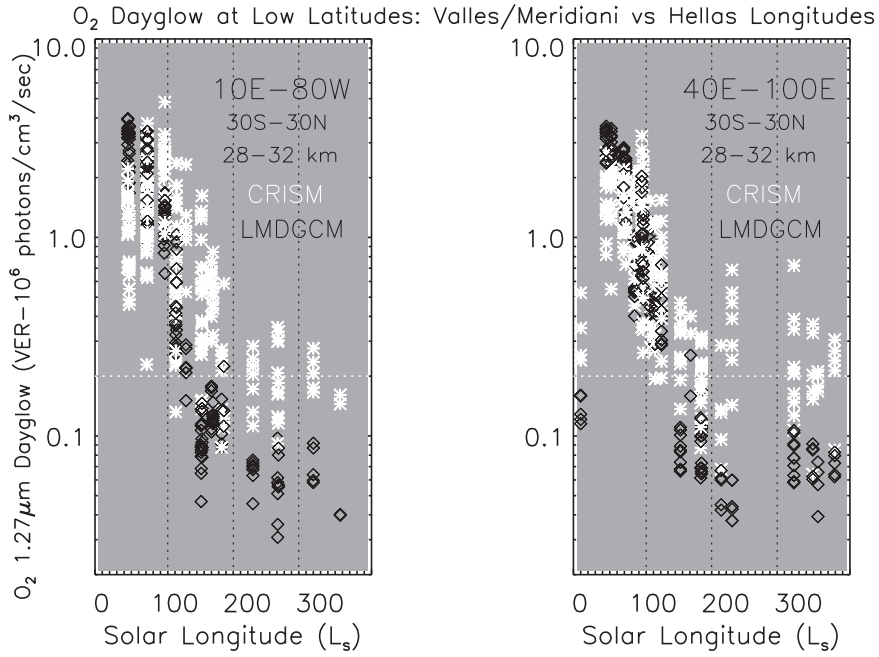

Fig. 7. Seasonal (L_s) variations in CRISM retrieved (white asterisks) and LMDGCM simulated (black diamonds) $O_2(^1\triangle_g)$ VER at 28–32 km altitudes and 30S–30N latitudes over Tharsis/Meridiani (left panel) versus Hellas Basin (right panel) surface longitudes. Increases in water vapor above 10–20 km altitudes after L_s=100° lead to sharp decreases in $O_2(^1\triangle_g)$ VER, which occur somewhat earlier in L_s for Tharsis/Meridiani longitudes. Simulated $O_2(^1\triangle_g)$ VER remain 2–3 times smaller than CRISM retrieved $O_2(^1\triangle_g)$ over L_s=120–360°. Vertical dotted lines indicate L_s values of 90°, 180°, and 270°.

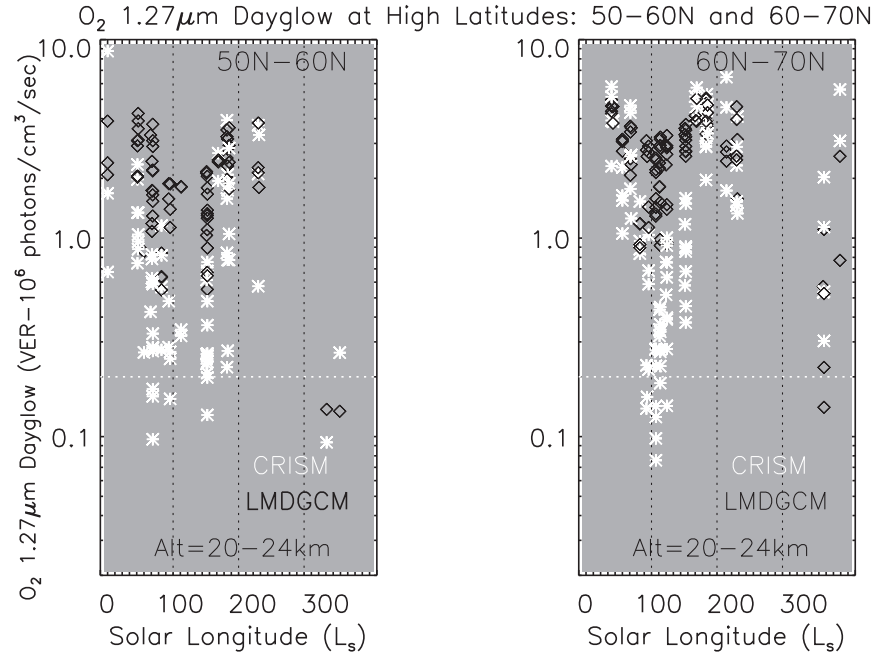

Fig. 8. Seasonal (L_s) variations in CRISM retrieved (white asterisks) and LMDGCM simulated (black diamonds) $O_2(^1\triangle_g)$ VER at 20–24 km altitudes are presented for high northern latitude ranges of 50–60N (left panel) and 60–70N (right panel). Model and observed peak $O_2(^1\triangle_g)$ VER in northern spring (L_s=0–50°) and fall (L_s=120–180°) are roughly similar. However, CRISM $O_2(^1\triangle_g)$ VER fall by a factor of 2–10 below LMDGCM modeled VER in northern summer (L_s=80–120°). Vertical dotted lines indicate L_s values of 90°, 180°, and 270°.

cap properties to match observed summer water columns in detail because the southern summer polar cap does not play a large role in regulating global water column behaviors. The southern summer $O_2(^1\triangle_g)$ CRISM measurements of Fig. 10 tend to reinforce that conclusion.

The extended behavior of the CRISM $O_2(^1\triangle_g)$ VER profiles over L_S of 60–310° (right panel of Fig. 9, left panel of Fig. 10) may provide partial resolution to existing disagreements between observed and modeled O_3 columns within the ACB and over low latitudes during perihelion. In particular, LMDGCM simulations of Mars low latitude O_3, tuned to reproduce observed Mars water column abundances versus latitude and season, fall roughly a factor-of-two below observed O_3 columns at Mars low latitudes (Lefèvre et al., 2008). Figs. 9 and 10 indicate that CRISM retrieved $O_2(^1\triangle_g)$ VER are several times larger than LMDGCM simulated $O_2(^1\triangle_g)$ VER, at low latitudes and above 10–20 km altitudes. Given the very

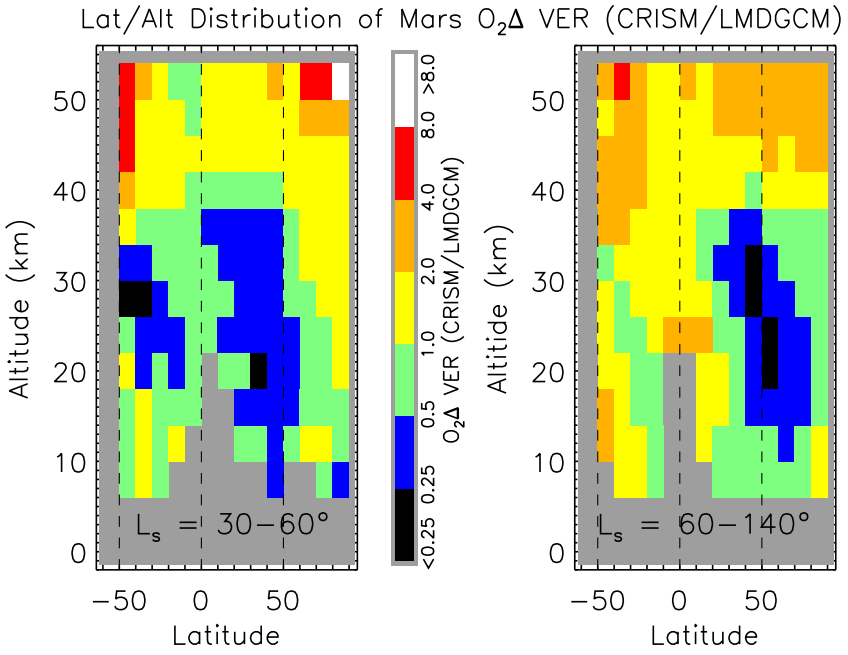

Fig. 9. The latitude/altitude distribution for the ratio of observed versus simulated $O_2(^1\Delta_g)$ VER (CRISM/LMDGCM) is presented for binned seasonal ranges corresponding to northern spring (L_s=30–60°; left panel) and northern summer (L_s = 60–140°; right panel). In northern spring (left panel), CRISM $O_2(^1\Delta_g)$ VER are 2–3 times smaller than LMDGCM values over ~15–35 km altitudes for 40S–60N latitudes; and 2–3 times larger than LMDGCM values above 40 km over all latitudes. In northern summer, CRISM $O_2(^1\Delta_g)$ VER are 2–3 times smaller than LMDGCM values over 15–35 km altitudes for 30N-90N latitudes; and 2–3 times larger than LMDGCM values above 40 km over all latitudes. Vertical dotted lines indicate latitude values of 50S, 0, and 50N.

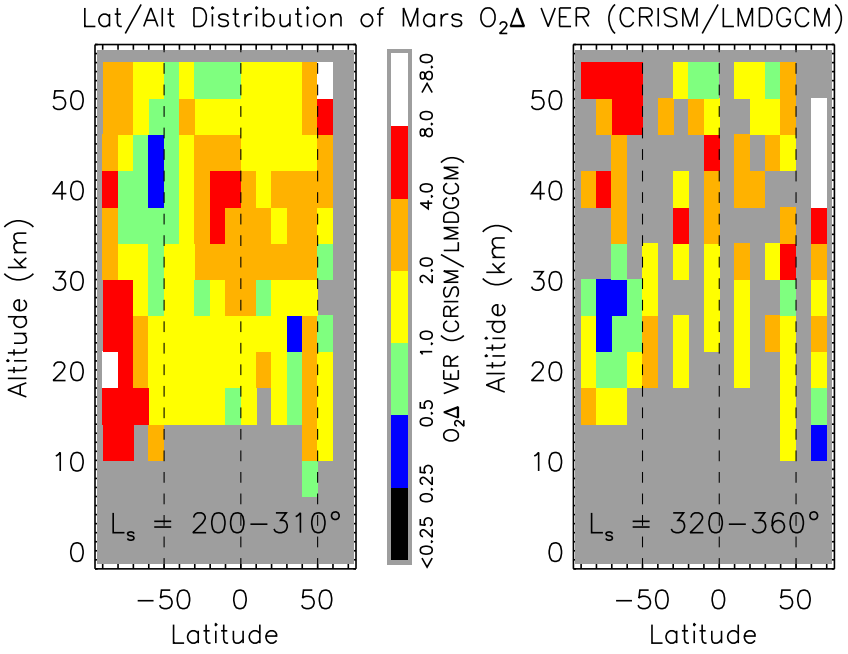

Fig. 10. The latitude/altitude distribution for the ratio of observed versus simulated $O_2(^1\Delta_g)$ VER (CRISM/LMDGCM) is presented for binned seasonal ranges corresponding to southern summer (L_s=200–310°; left panel) and southern fall (L_s=320–360°; right panel). In southern summer (left panel), CRISM $O_2(^1\Delta_g)$ VER are 3–7 times larger than LMDGCM values over 10–30 km altitudes above the southern polar region (90S-60S latitudes); and 2–4 times larger than LMDGCM values above 30–40 km for most latitudes. In southern fall (right panel), CRISM $O_2(^1\Delta_g)$ VER are comparable to LMDGCM values below 35 km for all latitudes; and 2–4 times larger than LMDGCM values above 35 km over all latitudes. Vertical dotted lines indicate latitude values of 50S, 0, and 50N.

direct relationship between $O_2(^1\Delta_g)$ emission and O_3 photolysis, model errors in the vertical distribution of O_3 over low latitude regions will contribute significantly to current model-data disagreements in Mars O_3 columns over low latitude regions. Furthermore, if we interpret $O_2(^1\Delta_g)$ VER (and O_3) in terms of atmospheric water vapor (as we do below), enhanced O_3 abundances above 10–20 km altitudes translate to significantly reduced water vapor abundances above 10–20 km. This may explain why observed low latitude H_2O_2 columns (where H_2O_2 is produced by H_2O photolysis) fall roughly a factor of 2 below LMDGCM simulated H_2O_2 columns (Encrenaz et al., 2015). Figs. 9 and 10 employ considerable seasonal (L_s) averaging in order to filter out the high degree of variability in both the observed and modeled $O_2(^1\Delta_g)$ VER profiles. Fig. 11 provides a quantitative view of this variability in

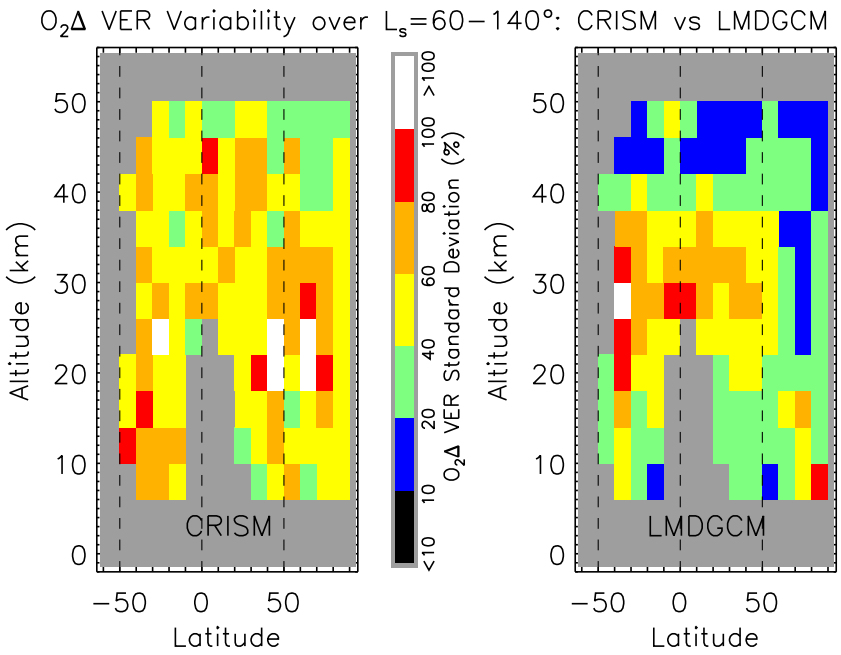

Fig. 11. The latitude/altitude distribution of 1σ variability, in terms of % of the mean, for CRISM (left panel) and LMDGCM (right panel) $O_2(^1\Delta_g)$ VER over northern summer (L_s=60–140°). Observed $O_2(^1\Delta_g)$ variability is typically 40–80%, and twice that for simulated $O_2(^1\Delta_g)$at higher altitudes and over northern high latitudes. Vertical dotted lines indicate latitude values of 50S, 0, and 50N.

CRISM observed (left panel) and LMDGCM simulated (right panel) $O_2(^1\Delta_g)$ VER versus latitude and altitude for the L_s=60–140° period of Fig. 9 (left panel). This period yields an optimum number of measurements per bin towards calculating the presented standard deviation of the $O_2(^1\Delta_g)$ VER distribution within each latitude/altitude bin (in percent of the mean). Fig. 11 reveals several aspects of the observed $O_2(^1\Delta_g)$ variability, relative to the model variability. Apart from the ~20–40 km region south of 50N latitude, where observed and modeled variaibilities are similar (~40-100%), observed variability is 2–3 times larger than modeled variability. Part of the increased variability in the CRISM $O_2(^1\Delta_g)$ VER reflects measurement/retrieval noise, although CRISM (and model) $O_2(^1\Delta_g)$ VER less than 2σ detection limits are excluded to minimize this effect. In any case, larger observed variability for the O_3 parent molecule is not unexpected, particularly in the planetary wave dominated mid-to-high latitude regions (Clancy et al., 2016).

The latitude/altitude distributions presented inFigs. 9 and 10 for CRISM versus LMDGCM $O_2(^1\Delta_g)$ VER indicate significant distinctions in modeled atmospheric water vapor, which we consider below. However, we first consider the effects of uncertain model chemistry regarding the collisional de-excitation of $O_2(^1\Delta_g)$ emission and heterogeneous loss of HO_x on cloud particles, both of which predominately concern $O_2(^1\Delta_g)$ emission below 20 km altitudes.

5.2. CO_2 collisional de-excitation of $O_2(^1\Delta_g)$ emission

A key uncertainty in interpreting Mars $O_2(^1\Delta_g)$1.27 μm observations is the uncertain efficiency of CO_2 collisions in quenching the $O_2(^1\Delta_g)$ electronically excited state. This process is expected to compete in the lower Mars atmosphere with radiative de-excitation, which takes place on an ~1 h timescale to produce the observed 1.27 μm emission. As discussed earlier, the rate coefficient for CO_2 collisional de-excitation of $O_2(^1\Delta_g)$, K_{CO2}, is not well determined from laboratory measurements. Burkholder et al. (2015) summarize existing laboratory constraints on K_{CO2}in terms of a very uncertain upper limit, based upon laboratory measurements predating 1985. Venus observational studies, based on Venus Express nightside $O_2(^1\Delta_g)$ limb measurements, are not specific for a determination of K_{CO2}(Gérard et al., 2013). A number of ground-based (Krasnopolsky, 2009) and spacecraft (Gagné et al., 2013; Guslyakova et al., 2016) observations of Mars column $O_2(^1\Delta_g)$ emission rates have been employed to further constrain $K_{CO2}$with mixed results. Guslyakova et al. (2016) performed the most complete such Mars column $O_2(^1\Delta_g)$ analysis for K_{CO2}, employing SPICAM column $O_2(^1\Delta_g)$ and O_3 measurements, to obtain a value of 0.73×10^{-20} cm^3sec^{-1}. The current CRISM retrievals for $O_2(^1\Delta_g)$ VER vertical profiles support several improvements over this analysis, including vertical resolution of the lower atmospheric region (altitude $\leq$ 20 km) most affected by CO_2 collisional de-excitation and explicit correction for atmospheric aerosol scattering/extinction. Neglect of $O_2(^1\Delta_g)$ emission extinction by aerosols leads to an overestimation of CO_2 collisional de-excitation, particularly when the relevant $O_2(^1\Delta_g)$ emission arises from the lowermost atmosphere.

Fig. 12 presents the accumulated (MY30-33, L_s=0–360°, 90S–90N) CRISM $O_2(^1\Delta_g)$ VER for aeroid altitudes $\leq$ 20 km, as compared to co-located (latitude, longitude, altitude)/co-temporal (LT, L_s) LMDGCM simulated $O_2(^1\Delta_g)$ VER. The upper and lower panels correspond to LMDGCM $O_2(^1\Delta_g)$ VER calculated for K_{CO2}= 0.73 (from Guslyakova et al., 2016) and 0.25(*currentwork*) × 10^{-20} cm^3sec^{-1}, respectively. In both cases, the LMDGCM heterogeneous chemistry is employed. Solid lines indicate average agreement between the observed and modeled $O_2(^1\Delta_g)$ VER, about which their uncorrelated variations should be distributed given average model-data agreement for lower atmospheric $O_2(^1\Delta_g)$. At least in this average sense, it is clear the current, lower value for K_{CO2}(lower panel) provides considerably better agreement than the larger value derived by Guslyakova et al. (2016). A qualification is the degree to which the model water vapor (hence, O_3) abundances below 20 km are consistent with observed conditions. The LMDGCM model is explicitly tuned to obtain agreement with observed water vapor columns, consistent with this assumption. Hence, the obtained water/O_3 column agreement is estimated to be better than 20% for the global/annual average represented in Fig. 12.

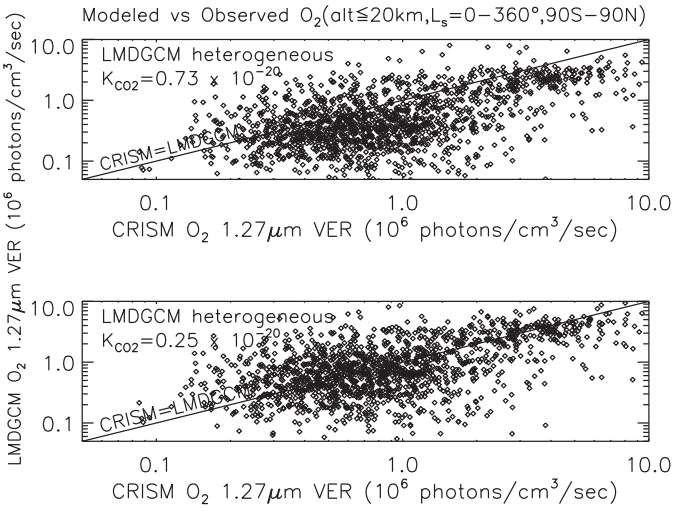

Fig. 12. CRISM retrieved $O_2(^1\Delta_g)$ VER are plotted against corresponding LMDGCM simulated values for all altitudes ≤ 20 km, for LMDGCM simulations using values of 0.73×10^{-20} (upper panel, from Guslyakova et al. (2016)) and 0.25×10^{-20} (lower panel, from current work) cm^3sec^{-1} for K_{CO2}, the CO_2 collisional de-excitation rate coefficient for $O_2(^1\Delta_g)$. In both cases, the LMDGCM simulations employ heterogeneous chemistry for HO_x on clouds.

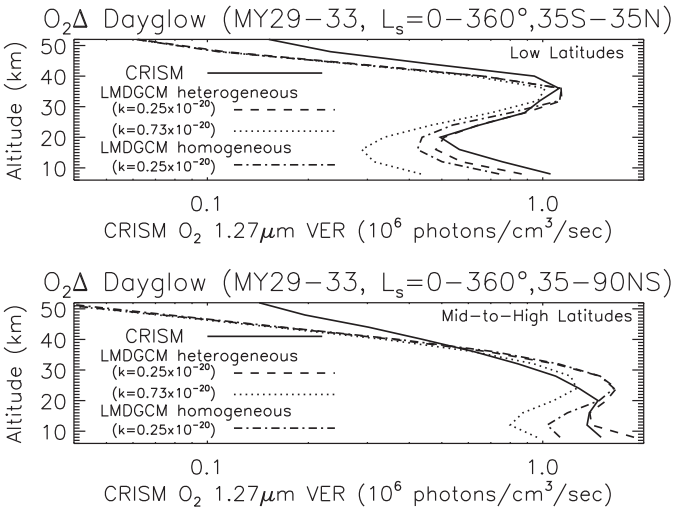

Fig. 13. CRISM (solid line) and LMDGCM (dashed and dotted lines) $O_2(^1\Delta_g)$ VER profiles, as averaged over low latitudes (upper panel, 35S-35N) and mid-to-high latitudes (lower panel, 35S-90S and 35N-90N), are compared for 3 model cases. LMDGCM simulations incorporating heterogeneous chemistry are presented for K_{CO2} values of 0.73×10^{-20} (dotted lines, from Guslyakova et al. (2016)) and 0.25×10^{-20} (dashed lines, from current work) cm^3sec^{-1}; and for LDMGCM simulations without heterogeneous chemistry (dash-dotted lines, 'homogeneous') for $K_{CO2} = 0.25 \times 10^{-20}$ cm^3sec^{-1}. CO_2 collisional de-excitation of $O_2(^1\Delta_g)(K_{CO2})$ and heterogeneous chemistry predominately affect $O_2(^1\Delta_g)$ VER below 20–30 km altitudes.

Another approach in comparing LMDGCM simulations as a function of model parameters regards averaged $O_2(^1\Delta_g)$ VER vertical profiles. Fig. 13 presents CRISM retrieved (solid lines) and LMDGCM modeled $O_2(^1\Delta_g)$ VER profiles as averaged for all paired data/model values within 35S–35N (top panel) and 35–90NS (bottom panel). In both cases, three model profiles are shown, for heterogeneous chemistry with $K_{CO2} = 0.25$ (dashed lines) and 0.73 (dotted lines) $\times 10^{-20}$ cm^3sec^{-1} and for purely homogeneous chemistry with $K_{CO2} = 0.25 \times 10^{-20}$ cm^3sec^{-1} (dash-dotted lines). The CRISM $O_2(^1\Delta_g)$ VER profiles of Fig. 13 demonstrate the average characters for such profiles over low versus high latitudes. Variations among the LMDGCM modeled profiles in both latitude ranges indicate that $O_2(^1\Delta_g)$ distinctions for homogeneous versus

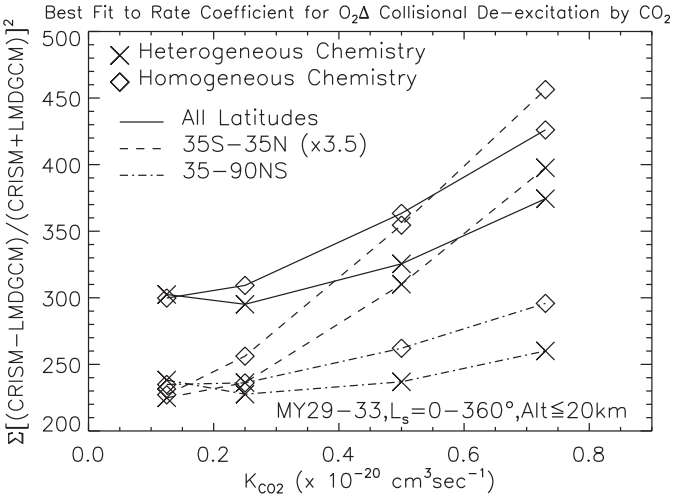

Fig. 14. The sum of the residuals squared (vertical axis) between all CRISM retrieved $O_2(^1\Delta_g)$ VER and corresponding LMDGCM simulated VER (for altitudes≤ 20 km), employing a range of CO_2 collisional de-excitation rate coefficients (K_{CO2}, horizontal axis), is plotted for both heterogeneous (X symbols) and homogenous (◇ symbols) photochemical simulations for latitude ranges of 35S–35N (dashed lines), 35–90NS (dash-dotted lines), and all latitudes combined (solid lines). Residuals are calculated relative to the sum of the modeled and observed values to obtain equal weighting across the 2 order-of-magnitude variations in $O_2(^1\Delta_g)$ VER. A best-fit value of $0.25 \pm 0.25 \times 10^{-20}$ cm^3sec^{-1} is derived for K_{CO2}.

heterogeneous chemistry are small (~10–20%), except for mid-to-high latitudes below 15–20 km altitudes (bottom panel, dashed versus dash-dotted lines).

Over both latitude ranges, CRISM average $O_2(^1\Delta_g)$ VER profiles are much better represented by LMDGCM $O_2(^1\Delta_g)$ simulations employing a value for K_{CO2} of 0.25 versus 0.73×10^{-20} cm^3sec^{-1}. This behavior holds for both homogeneous and heterogeneous chemistry simulations. Lefèvre et al. (2008) demonstrated that heterogeneous chemistry can improve agreement between SPICAM observed and LMDGCM simulated O_3 column densities, and that behavior is reflected in the improved $O_2(^1\Delta_g)$ model-data agreement in Fig. 13, primarily for mid-to-high latitudes.

We consider a larger comparison range for K_{CO2} in LMDGCM $O_2(^1\Delta_g)$ simulations in Fig. 14. In this case, we present the sum of the squared residuals between observed and modeled $O_2(^1\Delta_g)$ VER at or below 20 km (as in Fig. 12). Given the 2 order-of-magnitude variation in observed and modeled $O_2(^1\Delta_g)$ VER, it is necessary to weight these residuals by the sum of the observed and modeled $O_2(^1\Delta_g)$ VER at each point. Otherwise, the model-data residual sum is strongly biased to spatial/seasonal conditions of high $O_2(^1\Delta_g)$ VER. As in Fig. 13, we consider separate cases for high (dashed lines) and low (dash-dotted lines) latitudes, but also include the case for all latitudes combined (solid lines). For each of these cases, we consider LMDGCM $O_2(^1\Delta_g)$ simulations with (X symbols) and without (◇ symbols) heterogeneous chemistry. In all of these cases, the minimum in the sum of the squared residuals falls at (2 cases) or below (4 cases) a value of 0.25×10^{-20} cm^3sec^{-1} for K_{CO2}. In the latter 4 cases, a null value for K_{CO2} is preferred. LMDGCM simulations with heterogeneous chemistry lead to the 2 cases in which a minimum in the sum of the squared residuals occurs near $K_{CO2} = 0.25 \times 10^{-20}$ cm^3sec^{-1}, which also provides a better model-data correspondence in the O_3 source for $O_2(^1\Delta_g)$ dayglow. Nevertheless, such modeling uncertainties point to a conservative estimate for the rate constant of CO_2 collisional de-excitation of $O_2(^1\Delta_g)$, $K_{CO2} = 0.25 \pm 0.25 \times 10^{-20}$ cm^3sec^{-1}.

This value for K_{CO2} is roughly 3 times smaller than derived by Guslyakova et al. (2016). As indicated above, there are reasons to

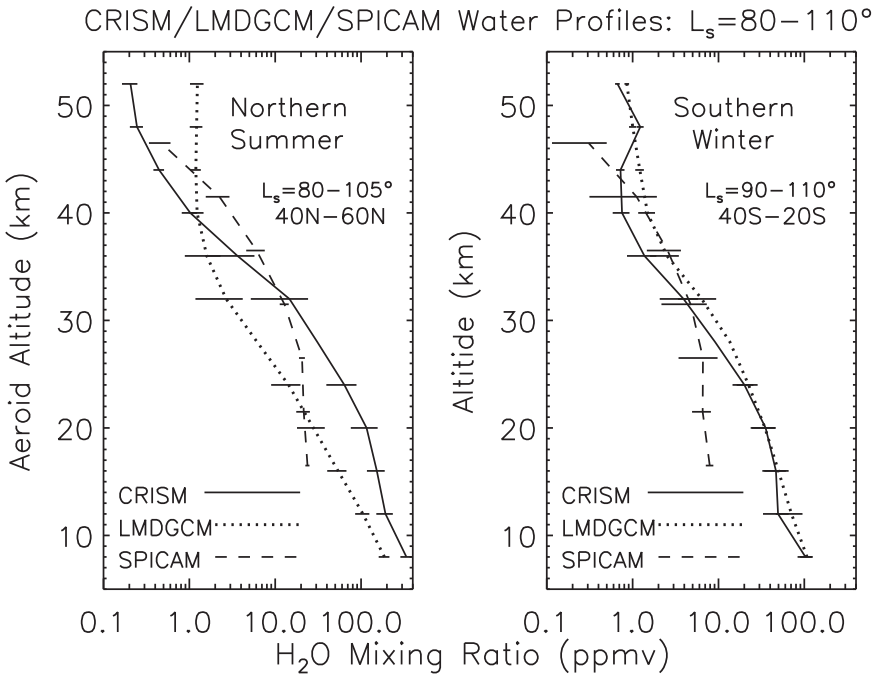

Fig. 15. Averaged CRISM derived (solid lines) and LMDGCM (dotted lines) water vapor mixing (ppmv) profiles are compared to average water vapor profiles from a set of SPICAM solar occultation retrievals (dashed lines) presented in Maltagliati et al. (2013), for L_s/latitude bins of 80–105°/40N–60N (left panel) and 90–110°/40S–20S (right panel). The SPICAM profiles are not co-located with the CRISM/model profiles and pertain to terminator local times, but do sample similar L_s and latitudes. Error bars refer to 1σ uncertainties in the calculated mean profiles, which incorporate ~10 and 15 individual CRISM/LMDGCM and SPICAM profiles, respectively, in each panel. CRISM and LMDGCM water profiles are distinctly different for the northern region (left panel), but quite similar for the southern region (right panel), as also exhibited in Fig. 16. Above 30 km (aeroid) altitudes, SPICAM water profiles are more similar to the CRISM derived values over northern latitudes, and similar to both CRISM and LMDGCM values over southern latitudes. SPICAM retrieved water values below 30 km in both latitude ranges approach constant mixing ratios, in disagreement with CRISM and LMDGCM behaviors.

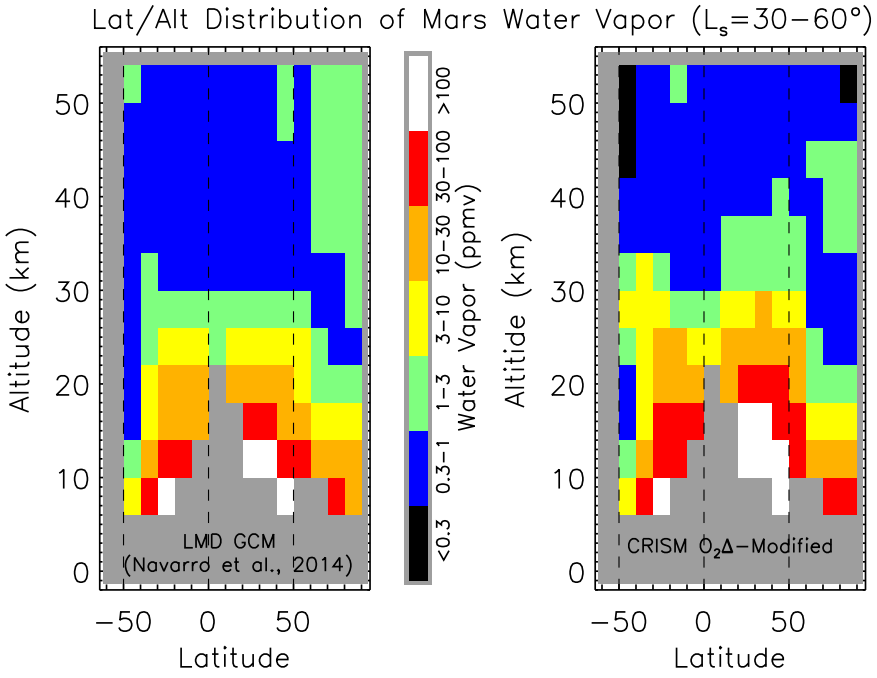

Fig. 16. The latitude/altitude distributions of LMDGCM simulated (left panel) and CRISM-derived water vapor (right panel), as averaged over the L_s=30–60° period. CRISM-derived water vapor is constructed by scaling LMDGCM simulated water vapor by the ratio of LMDGCM simulated to CRISM retrieved $O_2(^1\Delta_g)$ VER. The LMDGCM simulation employs heterogeneous chemistry and a value of 0.25×10^{-20} cm^3sec^{-1} for K_{CO2}. The CRISM derived water vapor distribution for this northern spring season is 2–4 times reduced above 40 km altitudes and 2-3 times increased over 15–35 km altitudes, relative to the LMDGCM water vapor distribution. Vertical dotted lines indicate latitude values of 50S, 0, and 50N.

expect that the CRISM profile retrievals for $O_2(^1\triangle_g)$ VER better constrain K_{CO2}relative to $O_2(^1\triangle_g)$ column measurements employed by Guslyakova et al. (2016), including the effects of aerosol extinction. However, it is not clear that such distinctions can account for a factor-of-three difference in retrieved K_{CO2}values. It is beyond the scope of the current analysis to explain this discrepancy in detail, but it is worth pointing out that the rapid rise in model-data summed residuals shortward of $K_{CO2}= 0.4 \times 10^{-20}$ cm^3sec^{-1}, as presented in Fig. 3 of Guslyakova et al. (2016), is inconsistent with its expected asymptotic behavior as presented in the current Fig. 14. Such small values in K_{CO2}lead to decreasing importance for $O_2(^1\triangle_g)$ de-excitation by CO_2 collisions, relative to baseline de-excitation rates associated with radiative relaxation (*i.e.*, $O_2(^1\triangle_g)$1.27 μm dayglow).

6. CRISM derived mars water vapor distributions

Comparisons of the CRISM retrieved and LMDGCM simulated $O_2(^1\triangle_g)$ VER distributions in altitude, latitude, and season (L_s) were presented in Figs. 9 and 10. The LMDGCM simulated $O_2(^1\triangle_g)$ VER were shown to exhibit a simple inverse dependence on the simulated water vapor abundance over the ~ two order-of-magnitude variability for Mars $O_2(^1\triangle_g)$ VER within a fixed region and period (right panel of Fig. 5). This inverse relationship is applied to scale LMDGCM simulated water vapor profiles by profiles of model/observed $O_2(^1\triangle_g)$ VER ratio profiles to generate CRISM derived water vapor profiles. In terms of systematic errors, the two key assumptions in this scaling are that the relationship between $O_2(^1\triangle_g)$ VER and O_3 abundance is well established, and that ratios between model and observed O_3 abundances are inversely related to ratios between model and observed water vapor abundances. At altitudes below ~20 km, the first assumption does depend on the modeled CO_2 collisional de-excitation rate coefficient for $O_2(^1\triangle_g)$, as derived above. A factor-of-two error in that rate coefficient contributes a ~20% error in scaled water vapor at an altitude of 15 km, fairly independent of season and latitude. The second assumption is primarily limited by the degree to which heterogeneous chemistry affects Mars O_3 abundances. Currently, the role of HO_x heterogeneous recombination on cloud particle surfaces remains an open question for high latitude O_3 abundances as this process is biased in models by unrealistically high polar hood cloud optical depths (Clancy et al., 2016). Nevertheless, the difference between heterogeneous and homogeneous model simulations of high latitude O_3 abundances (or $O_2(^1\triangle_g)$, see Fig. 13) below 15 km altitudes can be interpreted to introduce 30% uncertainties in CRISM derived water vapor abundances for these same high latitude regions.

We emphasize that both of these model-dependent uncertainties primarily affect CRISM derived water profiles below 20 km altitudes, and the latter error source is restricted to high latitudes. Systematic uncertainties for CRISM retrieved water vapor abundances above 20 km are of order 10–20%, as contributed by laboratory uncertainties in rate coefficients and photolysis cross sections associated with O_3 photochemistry and for the spontaneous $O_2(^1\triangle_g)$ emission coefficient. Statistical uncertainties of order 20% (1σ) also impact CRISM derived water vapor profiles above 20 km, as contributed by measurement/retrieval error and atmospheric variations within the latitude/L_s bins of averaging. All of these uncertainties fall well below the key departures between average LDMGCM simulated and CRISM derived water vapor profiles presented below (and suggested in $O_2(^1\triangle_g)$ differences presented in Figs. 9 and 10).

6.1. CRISM - SPICAM SOIR water profile comparisons

CRISM derived water profiles are compared to LMDGCM simulated profiles, for the most part, because there are very few Mars water vapor profile measurements appropriate for purely observational comparisons. Such comparisons require significant profile averaging over similar latitude/L_s bins to obtain representative averages in the context of large temporal/spatial variability for Mars water vapor profiles. We obtain two such comparisons, presented in Fig. 15, employing a set of SPICAM solar occultation infrared (SOIR) profile retrievals published in Maltagliati et al. (2013). The selected profiles correspond to an L_s range of 80–110° for latitude ranges of 40N–60N (left panel- northern summer) and 40S–20S (right panel- southern winter). Roughly 15 individual SPICAM profiles have been averaged in each case, the error bars indicate the 1σ in the profile average (dashed lines), based on the variance among the individual profiles. Only a few SPICAM profiles present water values at the lowest plotted level (15 km), which leads to unrealistic error limits for this value. We also note that SPICAM profiles presented in Maltagliati et al. (2013) for an L_s range of 213–272° generally refer to altitudes above 40 km and also do not lead to a sufficient number of comparison CRISM observations.

Roughly 10 co-registered LMDGCM and CRISM derived water vapor profiles are averaged to form their respective profile averages for each of the latitude/L_s ranges in Fig. 15, and their presented error bars refer to the 1σ uncertainties in these average temperature profiles. In general terms, the LMDGCM (dotted lines) and CRISM (solid lines) water profiles of Fig. 15 agree fairly closely for the southern winter latitude bin (right panel). However, they exhibit significant differences (factors of three) that vary with altitude over 15–55 km for the northern summer latitude range (left panel). These differences can be drawn by inspection of the latitude/altitude contour map of CRISM/LMDGCM $O_2(^1\triangle_g)$ VER ratios for the same latitude ranges, as presented for the L_s=60-140° period in Fig. 9, right panel. It is noteworthy that the vertical structure or shape of the LMDGCM and CRISM derived water profiles are quite similar for both latitude ranges, which is not the case for the SPICAM solar occultation profiles (dashed lines). Both SPICAM profiles exhibit a constant water vapor mixing ratio below ~30 km, which is not obviously consistent with observed water columns. SPICAM water abundances above 30 km are somewhat more consistent with CRISM derived versus LMDGCM simulated water abundances for the northern summer latitude range (left panel). Over the same altitude range, SPICAM water values fall between the LMDGCM and CRISM values for the southern winter latitude average. Overall, the SPICAM water mixing profiles are similar to the CRISM and LMDGCM water mixing profiles to within factor-of-two above 25–30 km altitudes. Below 25 km altitudes, SPICAM water values fall increasingly below CRISM and LMDGCM values.

Two additional qualifications apply to the SPICAM water profiles of Fig. 15. Firstly, they are adjusted to aeroid heights from their surface height scale presented in Maltagliati et al. (2013), employing a +3.5 km shift for the northern latitude bin and a –1.5 km shift for the southern latitude bin. Secondly, SPICAM solar occultation measurements refer to terminator local times, whereas the CRISM and LMDGCM local times fall near 3 pm. Clouds exhibit strong local time variations that will force local time variations in water vapor profiles, although these variations are not very specific to terminator local times (Hinson and Wilson, 2004). In any case, Fig. 15 is admittedly an inadequate observational basis for validating the CRISM derived water vapor retrieval. Currently there are limited opportunities for comparison, although the orbit insertion of the ExoMars Trace Gas Orbiter (TGO) in October of 2016 promises much improvement on this front. However, in the near term CRISM derived water vapor profiles constitute a unique global

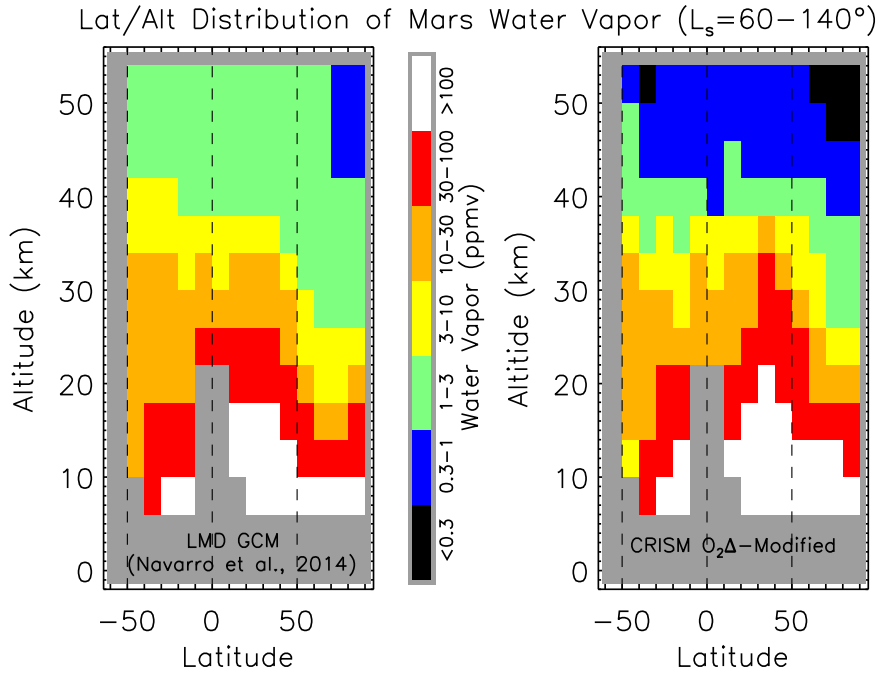

Fig. 17. The latitude/altitude distributions of LMDGCM simulated (left panel) and CRISM-derived water vapor (right panel), as averaged over the L_s=60-140° period. CRISM-derived water vapor is constructed by scaling LMDGCM simulated water vapor by the ratio of LMDGCM simulated to CRISM retrieved $O_2(^1\Delta_g)$ VER. The LMDGCM simulation employs heterogeneous chemistry and a value of 0.25×10^{-20} cm^3sec^{-1} for K_{CO2}. The CRISM derived water vapor distribution for this northern summer season is 2-3 times reduced above 35–40 km altitudes and water vapor is more strongly confined to the northern hemisphere, relative to LMDGCM simulated water vapor abundances. Over 20–35 km altitudes (within the ACB), peak water vapor abundances shift from low latitudes to northern mid-to-high latitudes. Vertical dotted lines indicate latitude values of 50S, 0, and 50N.

observational description of the vertical distribution of water vapor versus Mars season.

6.2. CRISM - LDMGCM water profile comparisons

Figs. 16–19 employ the inverse model relationship between $O_2(^1\Delta_g)$ VER and water vapor of Fig. 5 to characterize changes to the globally LMDGCM simulated water vapor distributions implied by the averaged CRISM/LMDGCM ratios for $O_2(^1\Delta_g)$ VER Figs. 9 and 10). In this case, the unmodified LMDGCM water vapor distribution in latitude/altitude (left panels) is compared to the modified model water vapor distribution (right panels), as scaled by the ratio of LMDGCM/CRISM $O_2(^1\Delta_g)$ VER in each latitude/altitude bin for L_s periods of 30–60° (Fig. 16), 60–140° (Fig. 17), 200–310° Fig. 18), and 320–360° (Fig. 19). The CRISM derived water vapor mixing ratios are presented in tabular form in an Appendix to this paper, including values for the L_s=140–200° seasonal range.

For the northern spring/summer periods represented inFigs. 16 and 17, two key modifications of the baseline (Navarro et al., 2014) LMDGCM water vapor distributions (left panels) result from scaling by CRISM $O_2(^1\Delta_g)$ VER measurements. Drier conditions (by 50–75%) result for altitudes above 35–40 km, and water vapor abundances below 30–35 km become much more strongly confined to the northern hemisphere. In the case of the L_s = 60–140° period (Fig. 16), the north-to-south latitudinal gradient in water vapor is actually reversed from the latitudinal gradient of the baseline LMDGCM water vapor distribution at 10–30 km altitudes. This suggests that the role of aphelion cloud belt (ACB) coupling with the solsticial Hadley circulation to restrict southward transport of water released by the sublimating northern ice cap (Clancy et al., 1996) is more efficient than currently simulated by the model. Both radiative and microphysical aspects of clouds affect the meridional transport of atmospheric water. As shown in Fig. 8 of Navarro et al. (2014), radiative forcing by the ACB acts to confine northern summer atmospheric water in a manner quite similar to that exhibited in Fig. 17. Vertical confinement of atmospheric water through cloud particle fall also restricts meridional transport in the southward (towards the summer hemisphere) upper branch of the solsticial Hadley circulation (Montmessin et al., 2004; Navarro et al., 2014). The application of observational constraints for modeling both of these processes is currently limited to atmospheric temperatures (Madeleine et al., 2012) and column water and cloud abundances (Navarro et al., 2014). Vertical profile measurements of cloud opacity (McCleese et al., 2010; Smith et al., 2013) and water vapor (here) should provide further discrimination, particularly in terms of cloud microphysical properties such as cloud particle size and nucleation efficiency.

The $O_2(^1\Delta_g)$ scaled water vapor distribution for the southern summer period of Fig. 18 (right panel) indicates 2–4 times less water vapor above 20 km altitudes for all latitudes in comparison to the model distribution (left panel). These CRISM derived decreases in atmospheric water vapor peak at factors of 5–6 above southern high latitudes relative to the baseline LMDGCM simulation. As mentioned earlier, this change lies well above the ~50% model overestimation relative to observed water columns for this region. As this is the L_s period for which water column measurements show increases associated with water release from the exposed southern polar ice cap (Smith, 2004), it appears that this water vapor is not efficiently transported above the lower scale height at this time. On a more global scale, the south-to-north hemispheric gradient of upper level water vapor is reversed between the CRISM derived and the LMDGCM simulated water vapor distributions. The effect is more subtle than for northern summer as it occurs at higher altitudes (~30–45 km), corresponding to the higher altitude of optically thin water ice clouds that are the southern summer (perihelion) equivalent of the ACB (see Fig. 21, also McCleese et al., 2010).

CRISM limb coverage is considerably less dense over the southern early fall period of Fig. 19 (L_s=320–360°). Average CRISM de-

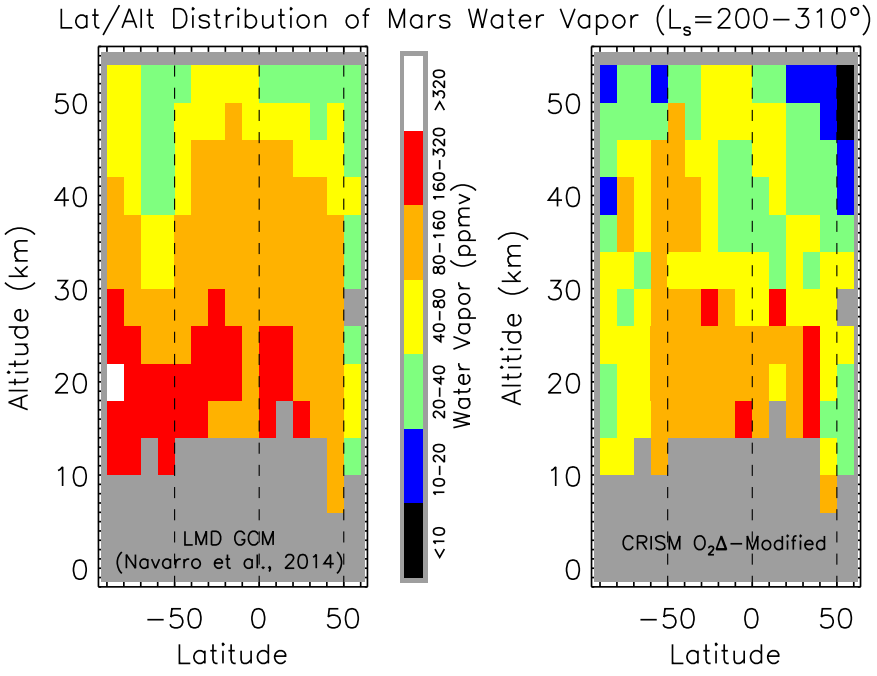

Fig. 18. The latitude/altitude distributions of LMDGCM simulated (left panel) and CRISM-derived water vapor (right panel), as averaged over the L_s=200–310° period. CRISM-modified water vapor is constructed by scaling LMDGCM simulated water vapor by the ratio of LMDGCM simulated to CRISM retrieved $O_2(^1\triangle_g)$ VER. The LMDGCM simulation employs heterogeneous chemistry and a value of 0.25×10^{-20} cm^3sec^{-1} for K_{CO2}. Relative to LMDGCM simulated water vapor, the CRISM derived water vapor abundances in this southern summer season are 2-3 times reduced at altitudes above 30 km. Over 10–30 km altitudes, CRISM derived water vapor falls 6 times lower than simulated values over southern high latitudes, and generally lies a factor of 2 lower over all latitudes. Vertical dotted lines indicate latitude values of 50S, 0, and 50N.

rived water vapor in the lower atmosphere remains similar to the baseline LMDGCM simulated water vapor, though perhaps with a larger south-to-north gradient implied by the CRISM $O_2(^1\triangle_g)$ VER. It also appears that upper level water vapor, above 35–40 km altitudes, is a factor of 2-3 reduced in the CRISM derived water vapor distribution.

At least two areas of disagreement between LMDGCM simulated and CRISM derived water vapor profiles extend over most of the Mars year, based on Figs. 16–19. CRISM derived water vapor abundances above 40 km are generally 2-3 times lower than simulated abundances over the full ranges of latitudes observed. The LMDGCM water vapor simulations present high supersaturation ratios for this region that may be unrealistic. However, these high supersaturation ratios are present during aphelion but not perihelion seasons, and so cannot account for the observed annual constancy of this LMDGCM-CRISM difference (see following section). Perhaps another factor is that less effective summer-to-winter cross hemispheric transport of atmospheric water, based on the CRISM derived aphelion and perihelion distributions (above), also reduces upper level transport of water vapor in the global Hadley circulation.

At lower altitudes (15–35 km) and latitudes (30S–30N), CRISM derived water vapor abundances are 2-3 times lower than LMDGCM simulated abundances for most of the Mars year. As mentioned earlier, such a change in the low latitude vertical distribution of water vapor would improve model-data disagreements in low latitude column O_3 (Lefèvre et al., 2008) and H_2O_2 (Encrenaz et al., 2015), where heterogeneous cloud chemistry is no longer expected to be effective (Clancy et al., 2016). Cloud microphysics in the ACB is a plausible process for reduction of water vapor above 15 km in the aphelion season. It is less clear what process is responsible in the perihelion season, although it does appear that water vapor evolved from the southern summer ice cap is less effectively transported above 10 km altitudes at high southern latitudes and so may depress water abundances above 10 km globally.

6.3. Water saturation ratios and their correspondence with cloud mixing ratios

Two additional aspects of the vertical distribution of water vapor in the Mars atmosphere are considered in the following; the distribution of water vapor saturation conditions implied in the LMDGCM simulated and CRISM derived water vapor vertical distributions, and the degree to which LMDGCM modeled and CRISM retrieved cloud profiles correlate with their distinct water vapor saturation distributions. Given that the employed (Navarro et al., 2014) LMDGCM model for Mars atmospheric water explored water vapor supersaturation in the context of recent SPICAM solar occultation studies (Maltagliati et al., 2011; 2013), it is instructive to consider how the seasonal/global occurrence of highly saturated water vapor changes for the CRISM derived water vapor vertical distributions. However, it is important to stress that model atmospheric temperatures are used to calculate saturation ratios for both the LMDGCM and CRISM water profile distributions. A 3 K temperature uncertainty leads to roughly a factor of two change in calculated water saturation ratios, and model temperature comparisons to Mars Climate Sounder (MCS) temperature profiles (McCleese et al., 2010) show considerably larger differences than this (Maltagliati et al., 2013). In fact model simulations for different Mars Year dust loading conditions exhibit temperature differences much larger than this. The lack of coincident temperature and water vapor profile measurements is a significant limitation in identifying or interpreting water vapor supersaturation in the Mars atmosphere. Hence our saturation ratio comparisons focus on relative changes in saturated water vapor conditions rather than supersaturation specifically.

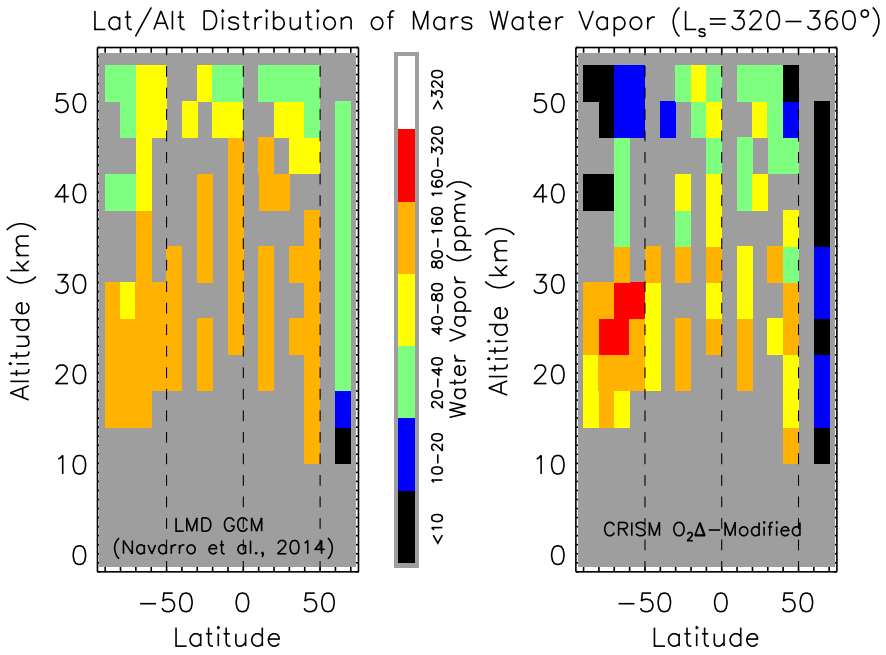

Fig. 19. The latitude/altitude distributions of LMDGCM simulated (left panel) and CRISM-modified water vapor (right panel), as averaged over the L_s=320–360° period. CRISM derived water vapor is constructed by scaling LMDGCM simulated water vapor by the ratio of LMDGCM simulated to CRISM retrieved $O_2(^1\Delta_g)$ VER. The LMDGCM simulation employs heterogeneous chemistry and a value of 0.25×10^{-20} cm^3sec^{-1} for K_{CO2}. Although coverage in this southern fall season is limited, the CRISM derived water vapor distribution for this southern summer season appears to be 2-3 times reduced above 30 km altitudes, and roughy unchanged over 10–30 km altitudes for all latitudes. Vertical dotted lines indicate latitude values of 50S, 0, and 50N.

Figs. 20 and 21 present comparisons between the LMDGCM simulated and CRISM derived water saturation ratios (upper panels) and retrieved cloud (water ice) mixing ratios (lower panels, scaled by atmospheric density) for northern summer (L_s=60–140°) and southern summer (L_s=200–310°) periods, respectively. The LMDGCM and CRISM cloud mixing ratios presented in the bottom panels of Figs. 20 and 21 have been scaled to obtain rough agreement of peak cloud values within the ACB, as their units are distinct (water ice molecular density versus water ice opacity). MCS water ice mixing ratios, in similar units to CRISM values, are shown to be in general agreement with CRISM retrievals (Smith et al., 2013). The presented water saturation ratios are calculated with LMDGCM simulated temperatures, for both LMDGCM simulated (left panels) and CRISM derived (right panels) water vapor abundances, employing the Goff-Gratch vapor saturation formulation adopted in Maltagliati et al. (2013). Conditions of near-saturation to saturation are indicated by colors of green-to-yellow, conditions of super saturation by colors of orange-red-white. Altitude-latitude regions of high water vapor saturation are prominent, for both LMDGCM and CRISM water abundances, during both aphelion periods (Fig. 20; and L_s=30–60° period not shown); whereas saturated conditions are much less prominent during the L_s=200–310° period (Fig. 21). This L_s saturation ratio dependence reflects the ~20 K orbital variation in global Mars atmospheric temperatures associated with the eccentric Mars orbit, even though larger water vapor mixing ratios characterize the vertically extended Mars perihelion (Fig. 18) versus aphelion (Fig. 17) atmosphere.

The CRISM derived water vapor distributions lead to enhancement of this orbital variation in global water vapor saturation conditions for the Mars atmosphere. Changes between LMDGCM and CRISM water vapor saturation distributions are opposite in sign for the aphelion (Fig. 20) versus perihelion (Fig. 21) periods. Higher saturation ratios at northern mid-to-high latitudes are exhibited by CRISM versus LMDGCM aphelion water vapor distributions (white ellipse region in Fig. 20), which is roughly consistent with SPICAM supersaturation measurements reported in Maltagliati et al. (2011). These CRISM increases in northern hemisphere aphelion water vapor saturation ratios are accompanied by increased CRISM cloud mixing ratios relative to LMDGCM simulated values, as presented in the lower panels of Fig. 20 within co-located white ellipse regions. In contrast, lower saturation ratios at southern polar latitudes are exhibited by CRISM versus LMDGCM perihelion water vapor distributions (Fig. 21a). The southern polar region also exhibits significantly reduced CRISM versus LMDGCM cloud mixing ratios in the lower panels of Fig. 21. Hence, there is a rough correlation between CRISM-to-LMDGCM changes in water vapor abundance/saturation and cloud mixing ratio over northern summer and southern summer latitudes, although the changes are opposite in sign for these two periods. In this respect, CRISM retrieved distributions of Mars clouds are consistent with CRISM derived water vapor distributions.

Modeling the detailed vertical distribution of Mars water vapor versus latitude and season (and longitude, which we do not address due to limited coverage) adds additional complexities to the already complex problem of modeling the global distribution of water vapor columns (e.g., Richardson and Wilson, 2002; Montmessin et al., 2004; Navarro et al., 2014; Steele et al., 2014). All of these existing modeling studies have shown the importance of water ice clouds on influencing the water column distribution in season and latitude, more recently including the effects of cloud radiative forcing on transport and polar ice sublimation rates (Haberle et al., 2011; Madeleine et al., 2012; Urata and Toon, 2013; Navarro et al., 2014). Cloud influences on water vertical profiles are, not surprisingly, more profound given the effects of altitude decreasing temperatures on water vapor saturation ratios, uncertainties in cloud nucleation and particle sizes, and strong diurnal variations in the vertical structure of Mars clouds (Hinson and Wilson, 2004). In this respect, the differences between the LMDGCM simulated and CRISM derived water vapor and cloud vertical distributions in season and latitude are not surprising. Indeed, given

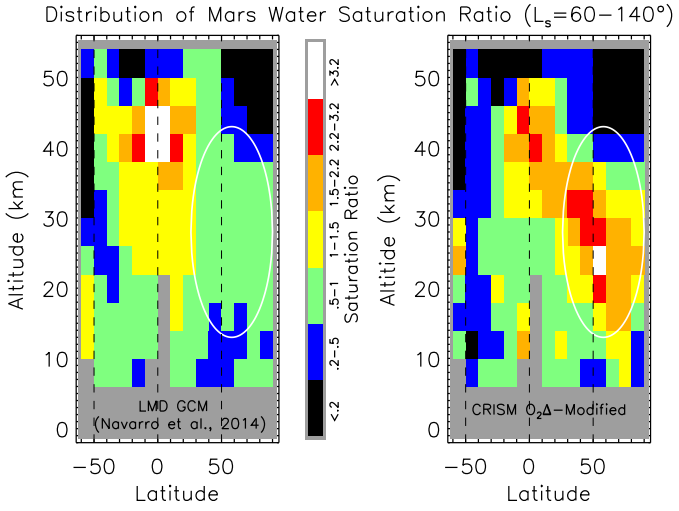

a LMDGCM (left) and CRISM (right) Water Saturation Ratios

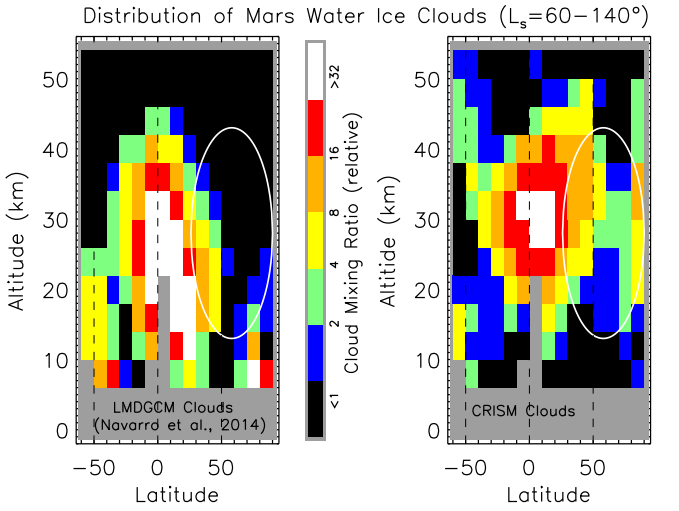

b LMDGCM (left) and CRISM (right) Cloud Mixing Ratios

Fig. 20. The latitude/altitude distributions of LMDGCM simulated (left panel) and CRISM derived (right panel) water vapor saturation ratios (top panels) and water ice cloud mixing abundance (bottom panels), as averaged over the L$_s$=60–140° period. CRISM and LMDGCM water saturation ratios are calculated with model (LMDGCM) temperature profiles, and primarily reflect CRISM water vapor abundance increases at northern mid-to-high latitudes (Fig. 16). CRISM cloud mixing ratios (scaled to provide average model-data agreement for the low latitude ACB) exhibit increases over LMDGCM simulated values, over these same regions (indicated by white ellipses in each panel). Regions of high water super-saturations (orange to white colors) may reflect incorrect (too cold) model temperatures, rather than strongly super-saturated conditions over such large scales. Vertical dotted lines indicate latitude values of 50S, 0, and 50N.

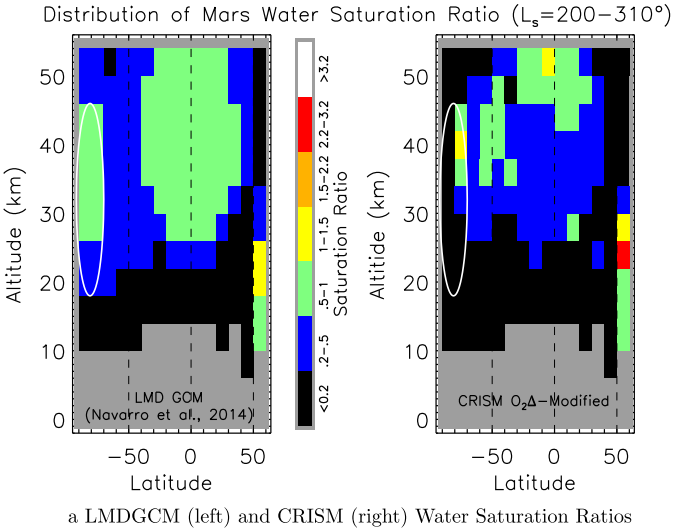

a LMDGCM (left) and CRISM (right) Water Saturation Ratios

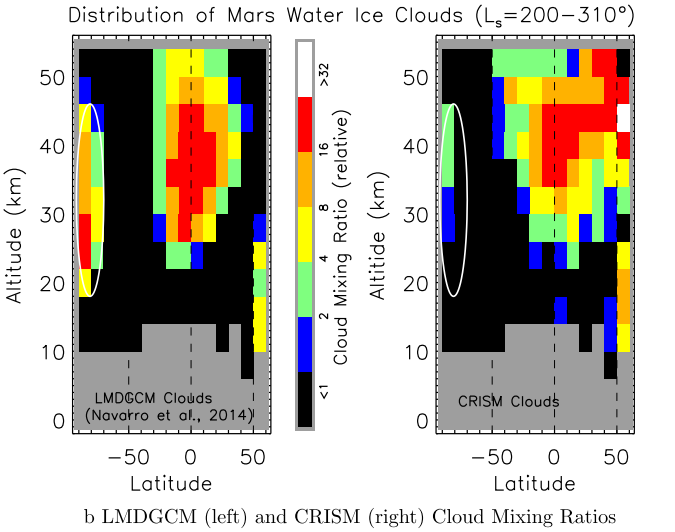

b LMDGCM (left) and CRISM (right) Cloud Mixing Ratios

Fig. 21. The latitude/altitude distributions of LMDGCM simulated (left panel) and CRISM-retrieved (right panel) water vapor saturation ratios (top panels) and water ice cloud mixing abundance (bottom panels), as averaged over the L$_s$=200–310° period. CRISM and LMDGCM water saturation ratios are calculated with model (LMDGCM) temperature profiles, and primarily reflect CRISM water vapor abundance decreases at southern polar and southern low latitudes (Fig. 17). In contrast to the aphelion period of Fig. 20, CRISM cloud mixing ratios and water saturation ratios exhibit distinct decreases over LMDGCM simulated values, over southern polar latitudes (indicated by the same white ellipse in each panel). Generally much lower water vapor saturation ratios are exhibited for this perihelion period, versus aphelion Fig. 20) and northern spring (not shown, but see Fig. 15) periods. Vertical dotted lines indicate latitude values of 50S, 0, and 50N.

the complex and uncertain set of atmospheric processes controlling Mars water vapor profile behavior, the level of model-data agreement is actually quite encouraging. However, the corollary of this encouragement is that it will not be easy to obtain diagnostic agreement between observed and modeled vertical distributions of water vapor and clouds in the Mars atmosphere.

One key step to obtaining this agreement is a more complete water profiling data set for the Mars atmosphere. The comparisons of modeled and CRISM derived Mars water vapor distributions presented in Figs. 16–21 constitute the first global assessment of modeled seasonal (L$_s$) and spatial (latitude) water profile distributions in the context of global measurements. This reflects a striking omission in Mars atmospheric observational studies with respect to profile measurements of water vapor, soon to be addressed by solar occultation and limb water vapor profiling from the ExoMars Trace Gas Orbiter (to begin mission observations in 2018).

7. Conclusions

The first globally extended set of Mars $O_2(^1\Delta_g)$ dayglow VER profiles (~1100) is retrieved based on CRISM near-IR limb spectral scans obtained over 2009–2016. Simultaneous $O_2(^1\Delta_g)$ and aerosol (dust and ice) vertical profile retrievals were performed employing spherical multiple-scattering RT. Solution $O_2(^1\Delta_g)$ VER profiles extend over 8 to 80 km altitude, 0–360° in L$_s$, and all sunlit lati-

tudes. These retrieved $O_2(^1\triangle_g)$ dayglow profiles were compared to co-located (latitude, longitude, altitude), co-temporal (L_s, LT) simulated $O_2(^1\triangle_g)$ VER from the LMDGCM photochemical code (Lefèvre et al., 2004; 2008), incorporating recent cloud microphysical modifications designed to improve observed-modeled water vapor column agreement (Navarro et al., 2014). These model-data comparisons for Mars $O_2(^1\triangle_g)$ VER provide: 1) a determination of the rate coefficient for CO_2 collisional de-excitation of $O_2(^1\triangle_g)(K_{CO2})$ and, 2) characterization of Mars' atmospheric water vapor distributions in latitude, altitude, and L_s relative to the LMDGCM simulated water vapor distributions.

For aeroid altitudes ≤20 km, Mars $O_2(^1\triangle_g)$ dayglow provides a sensitive measure of K_{CO2}. Based on the full set of such CRISM $O_2(^1\triangle_g)$ VER retrievals, a best-fit value of 0.25± 0.25 x 10^{-20} cm^3sec^{-1} is determined for K_{CO2}. The stated uncertainty includes both measurement and photochemical modeling error contributions. This value for K_{CO2} is ~3 times smaller than derived by Guslyakova et al. (2016) employing SPICAM $O_2(^1\triangle_g)$ column integrated measurements. The seasonal/spatial differences between observed and modeled $O_2(^1\triangle_g)$ VER are most reflective of model water vapor profile inaccuracies, due to the simple inverse relationship between $O_2(^1\triangle_g)$ VER and the local water vapor abundance over their two orders-of-magnitude variations in the Mars atmosphere. Based on this inverse relationship, latitude/altitude distributions for Mars atmospheric water vapor are presented for averaged L_s bins of 30–60°, 60–140°, 200–310°, and 320–360°. These CRISM derived water vapor distributions are constructed by scaling model (LMDGCM) water vapor distributions by the average ratio of LMDGCM modeled to CRISM observed $O_2(^1\triangle_g)$ VER within each latitude, altitude, and L_s bin. These L_s bin averaged latitude/altitude cross sections for Mars water vapor mixing ratio are also provided in tabular form in the Appendix at the end of this paper, in which the L_s=60–140° period is separated into two L_s bins (60–100° and 100–140°) and an L_s bin for 140–200° is added.

Several aspects of this CRISM derived water vapor distribution, relative to the LMDGCM water vapor distribution, are: 1) 2–3 times reduced water vapor above 35–40 km altitudes for all L_s periods, which may indicate less effective global transport of water vapor to these higher altitudes; 2) 2–3 times reduced water vapor mixing ratios between 15 and 35 km over low latitudes for all L_s periods, which likely contributes to current model-data disagreements for low latitude O_3 and H_2O_2 columns; 3) water vapor released from the northern spring/summer polar ice reservoirs that is more strongly confined to northern mid-to-high latitudes over 10–35 km altitudes, which may partly reflect more vigorous blocking of southward water transport by cloud microphysics and radiative forcing in the ACB than currently modeled (this behavior also appears less distinctly at higher altitudes during the southern summer); 4) 3–6 times reduced water vapor abundances at 10–30 km above southern summer polar ice reservoirs, indicating very limited vertical transport of water from south polar ice reservoirs that further limits their influence on global atmospheric water variations; 5) an enhanced orbital variation in global saturation conditions for Mars atmospheric water vapor; and 6) correlation of spatial distributions for CRISM water vapor changes with respect to the LMDGCM values, to spatial distributions for CRISM changes in cloud opacity with respect to LMDGCM values.

Many of these differences reflect the inherent difficulties in modeling sufficiently accurate or complete cloud microphysics in Mars GCM simulations. Nevertheless, the Navarro et al. (2014) LMDGCM simulations of Mars atmospheric water vapor distributions represent the most detailed representation of such microphysics in a Mars global climate model and provide a standard for future improvements. Another key to those improvements will be global, coincident profile measurements of Mars water vapor, clouds, and temperatures. Solar occultation and limb profiling measurements from the ExoMars TGO mission should provide this critical data set over 2018–2019.

Acknowledgements

We are indebted to the excellent MRO and CRISM operations staff for the collection and processing of CRISM limb observations presented here. Grant support for this work was provided by the NASA MDAP Program (under NASA contract award number NNX10AL61G).

Appendix A. Water profile tables

CRISM derived Mars Water Vapor Mixing Profiles (ppmv) are derived from retrieved CRISM $O_2(^1\triangle_g)$ profiles, as described above, through scaling of the LMDGCM water profiles Navarro et al. (2014) by the LMDGCM/CRISM ratio of $O_2(^1\triangle_g)$ volume emission rates (H_2O and $O_2(^1\triangle_g)$ are inversely proportional). Above 20 km altitudes, average uncertainties are 20% (1σ), as binned over 6 coarse seasonal (L_s- solar longitude) ranges. These include the L_s=140-200° period not discussed in the paper and the separation of the L_s=60-140° period into two L_s bins of 60–100° and 100–140°. Below 20 km altitudes, model assumptions contribute systematic uncertainties of order 20–30%. The latitude averaging bins of 10 degrees are centered on the provided latitudes. The longitudinal coverage is restricted to 110W-60E, and to a fixed local time of ~3 pm. Altitude levels in steps of 4 km are aeroid altitudes. Northern hemisphere latitudinal gradients in surface elevation may play a role in northern hemisphere latitudinal gradients in derived water vapor values at the lowest aeroid altitude levels (8–16 km). Values of −1 indicate insufficient measurements (<4) to provide a bin average value.

Table 2
Water vapor mixing (ppmv) profiles (aeroid altitudes): L_s=30-60°.

Alt	Latitude																	
(km)	−85	−75	−65	−55	−45	−35	−25	−15	−5	5	15	25	35	45	55	65	75	85
52	−1.0	−1.0	−1.0	−1.0	0.2	0.4	0.4	1.0	0.9	0.5	0.5	0.4	0.5	0.5	0.5	0.4	0.4	0.2
48	−1.0	−1.0	−1.0	−1.0	0.2	0.6	0.4	0.6	0.8	0.7	0.6	0.5	0.5	0.6	0.5	0.7	0.9	0.6
44	−1.0	−1.0	−1.0	−1.0	0.2	0.5	0.4	0.5	0.5	0.4	0.4	0.4	0.6	0.8	0.5	1.1	1.6	1.3
40	−1.0	−1.0	−1.0	−1.0	0.4	0.5	0.5	0.5	0.6	0.6	0.6	0.9	0.9	1.1	0.7	1.0	1.4	1.5
36	−1.0	−1.0	−1.0	−1.0	0.8	1.0	0.7	0.6	0.7	0.9	1.2	1.8	1.9	1.8	1.1	0.8	1.1	1.4
32	−1.0	−1.0	−1.0	−1.0	2.0	3.4	1.6	0.8	0.8	0.9	2.0	2.3	3.1	2.1	1.5	0.7	0.8	0.9
28	−1.0	−1.0	−1.0	−1.0	4.9	7.7	6.1	2.7	2.1	2.4	3.9	6.1	10.4	4.4	3.5	0.9	0.6	0.6
24	−1.0	−1.0	−1.0	−1.0	1.1	8.3	15.8	13.1	7.2	5.4	15.2	24.8	27.5	12.0	16.1	1.5	0.7	0.6
20	−1.0	−1.0	−1.0	−1.0	0.4	9.0	18.1	26.5	26.3	−1.0	16.9	42.6	63.6	33.9	32.5	3.1	1.8	1.1
16	−1.0	−1.0	−1.0	−1.0	0.9	7.2	42.5	42.9	43.0	−1.0	−1.0	101	100	78.9	77.6	9.6	5.6	4.5
12	−1.0	−1.0	−1.0	−1.0	2.2	20.5	67.4	66.9	−1.0	−1.0	−1.0	152	151	138	50.3	12.9	16.8	17.9
8	−1.0	−1.0	−1.0	−1.0	7.2	33.7	109	−1.0	−1.0	−1.0	−1.0	−1.0	−1.0	215	−1.0	−1.0	48.0	54.3

Table 3
Water vapor mixing (ppmv) profiles (aeroid altitudes): L_s=60–100°.

Alt	Latitude																	
(km)	−85	−75	−65	−55	−45	−35	−25	−15	−5	5	15	25	35	45	55	65	75	85
52	−1.0	−1.0	−1.0	−1.0	−1.0	0.2	0.2	0.5	0.5	0.3	0.5	0.3	0.3	0.3	0.3	0.2	0.3	0.1
48	−1.0	−1.0	−1.0	−1.0	−1.0	0.3	0.3	0.5	0.8	0.5	0.5	0.3	0.3	0.3	0.4	0.3	0.6	0.3
44	−1.0	−1.0	−1.0	−1.0	−1.0	0.3	0.4	0.6	0.5	0.4	0.6	0.4	0.4	0.5	0.6	0.7	0.7	0.4
40	−1.0	−1.0	−1.0	−1.0	−1.0	0.4	0.4	0.4	0.3	0.3	0.6	0.8	1.1	1.4	1.1	1.1	1.0	0.7
36	−1.0	−1.0	−1.0	−1.0	−1.0	0.8	0.6	0.6	0.6	0.5	1.2	3.3	5.0	5.8	2.5	1.7	1.4	1.0
32	−1.0	−1.0	−1.0	−1.0	−1.0	2.8	2.0	2.3	2.5	1.9	3.9	12.1	19.9	19.8	5.7	2.6	1.5	1.4
28	−1.0	−1.0	−1.0	−1.0	−1.0	10.6	5.8	4.3	4.2	4.2	7.5	19.3	32.6	38.6	11.5	5.1	2.3	2.4
24	−1.0	−1.0	−1.0	−1.0	−1.0	16.2	16.6	9.0	8.8	14.3	10.5	40.3	45.4	52.7	35.9	12.4	5.6	6.1
20	−1.0	−1.0	−1.0	−1.0	−1.0	18.9	39.5	27.4	−1.0	−1.0	−1.0	56.9	80.3	78.0	82.5	24.4	17.9	12.9
16	−1.0	−1.0	−1.0	−1.0	−1.0	20.4	40.6	46.3	−1.0	−1.0	−1.0	133	126	186	89.0	86.3	39.7	25.6
12	−1.0	−1.0	−1.0	−1.0	−1.0	28.1	43.9	119	−1.0	−1.0	−1.0	250	285	314	120	166	103	46.1
8	−1.0	−1.0	−1.0	−1.0	−1.0	44.8	86.7	218	−1.0	−1.0	−1.0	395	345	348	150	225	232	164

Table 4
Water vapor mixing (ppmv) profiles (aeroid altitudes): L_s=100–140°.

Alt	Latitude																	
(km)	−85	−75	−65	−55	−45	−35	−25	−15	−5	5	15	25	35	45	55	65	75	85
52	−1.0	−1.0	−1.0	0.8	0.8	0.4	0.8	1.2	1.1	1.1	0.9	0.6	0.5	0.6	0.8	0.6	0.2	0.4
48	−1.0	−1.0	−1.0	−1.0	2.1	1.3	1.5	1.6	1.1	1.8	1.4	0.8	0.6	0.7	0.6	0.7	0.2	0.3
44	−1.0	−1.0	−1.0	−1.0	2.0	2.1	2.0	1.2	1.1	2.0	1.8	1.4	1.3	1.4	1.0	0.7	0.3	0.6
40	−1.0	−1.0	−1.0	−1.0	3.2	2.4	3.0	2.2	2.0	2.8	4.5	4.1	4.1	3.9	2.2	1.3	0.7	0.9
36	−1.0	−1.0	−1.0	6.5	7.8	4.1	6.2	5.9	6.1	8.6	11.8	12.5	18.3	12.5	6.9	3.0	1.1	1.4
32	−1.0	−1.0	−1.0	22.3	28.8	7.4	10.2	11.7	12.0	9.4	14.9	24.7	47.8	30.1	18.4	5.6	2.1	2.2
28	−1.0	−1.0	−1.0	27.5	27.3	19.1	18.2	12.8	20.1	14.4	21.1	37.4	49.2	61.8	52.9	11.7	4.7	4.8
24	−1.0	−1.0	−1.0	26.0	39.4	29.5	46.6	15.5	30.1	23.7	25.1	41.4	98.2	98.7	65.8	20.7	11.8	9.8
20	−1.0	−1.0	−1.0	4.3	16.2	35.2	71.2	49.7	−1.0	−1.0	66.3	124	162	139	68.2	33.3	33.8	27.4
16	−1.0	−1.0	−1.0	2.0	12.7	35.3	72.2	67.9	−1.0	−1.0	116	208	187	158	90.6	58.0	87.8	65.8
12	−1.0	−1.0	−1.0	2.1	6.6	54.0	86.9	95.7	−1.0	−1.0	595	676	260	150	172	106	196	86.7
8	−1.0	−1.0	−1.0	−1.0	7.0	62.9	152	−1.0	−1.0	−1.0	−1.0	928	789	249	314	197	458	159

Table 5
Water vapor mixing (ppmv) profiles (aeroid altitudes): L_s=140–200°.

Alt	Latitude																	
(km)	−85	−75	−65	−55	−45	−35	−25	−15	−5	5	15	25	35	45	55	65	75	85
52	−1.0	−1.0	3.0	1.7	3.6	4.2	7.0	7.9	6.5	5.1	7.4	7.2	3.8	3.9	0.5	0.9	1.7	1.2
48	−1.0	−1.0	−1.0	10.7	2.5	9.9	11.2	11.5	6.8	10.4	13.8	25.4	6.2	5.8	1.0	0.3	0.4	0.4
44	−1.0	−1.0	3.2	11.1	1.0	14.8	17.8	11.0	9.6	16.1	22.8	28.9	18.0	17.2	1.9	0.5	0.3	0.3
40	−1.0	−1.0	3.7	24.1	19.7	13.1	26.9	19.6	22.0	26.7	26.8	36.9	42.2	34.8	3.2	1.3	0.7	0.6
36	−1.0	−1.0	22.4	42.9	12.7	20.1	58.0	23.2	20.6	29.2	37.7	47.4	68.2	67.8	3.9	2.0	0.6	0.4
32	−1.0	−1.0	11.3	145.8	50.8	35.0	45.0	32.6	33.8	26.4	52.7	50.8	68.9	149.0	4.5	1.5	0.5	0.3
28	−1.0	−1.0	2.6	78.8	50.0	64.7	46.3	38.8	24.0	39.0	51.2	71.1	83.8	152	5.6	0.6	0.4	0.2
24	−1.0	−1.0	1.5	38.8	59.0	65.1	58.0	94.7	66.7	53.4	84.1	105	53.9	103	7.9	0.3	0.2	0.1
20	−1.0	−1.0	3.4	33.0	35.9	54.1	76.9	135	124	181	124	87.5	75.9	70.8	11.6	0.4	0.3	0.0
16	−1.0	−1.0	9.5	62.5	106	64.0	100	122	155	259	164	114	168	66.9	16.1	1.7	0.8	0.0
12	−1.0	−1.0	−1.0	67.1	306	−1.0	155	147	215	−1.0	240	156	253	74.9	49.3	11.7	4.2	0.4
8	−1.0	−1.0	−1.0	−1.0	−1.0	−1.0	−1.0	−1.0	−1.0	−1.0	−1.0	−1.0	340	121	−1.0	35.3	−1.0	−1.0

Table 6
Water vapor mixing (ppmv) profiles (aeroid altitudes): L_s=200–310°.

Alt	Latitude																	
(km)	−85	−75	−65	−55	−45	−35	−25	−15	−5	5	15	25	35	45	55	65	75	85
52	17.6	23.4	27.7	19.3	39.5	23.5	57.3	49.2	65.7	37.1	28.0	15.5	11.8	13.1	3.0	−1.0	−1.0	−1.0
48	26.4	21.4	28.2	35.6	82.9	21.8	55.6	66.6	57.4	58.9	46.8	33.5	30.0	19.1	5.9	−1.0	−1.0	−1.0
44	20.1	56.1	43.3	101.0	83.1	42.5	46.0	33.3	36.7	55.1	52.4	38.3	36.9	33.1	10.2	−1.0	−1.0	−1.0
40	18.0	103.4	46.4	80.8	94.1	86.7	46.1	29.6	24.5	36.5	48.9	28.4	26.9	36.1	18.2	−1.0	−1.0	−1.0
36	29.9	94.2	51.8	99.2	101	127	45.8	31.9	36.5	38.6	34.5	52.1	43.9	28.9	26.7	−1.0	−1.0	−1.0
32	41.9	59.9	34.1	103	67.5	75.4	74.3	68.7	59.5	42.9	35.1	53.7	37.5	44.3	61.0	−1.0	−1.0	−1.0
28	47.1	36.3	54.5	93.2	81.9	87.1	−1.0	113	53.2	65.3	−1.0	67.3	63.9	64.7	−1.0	−1.0	−1.0	−1.0
24	50.2	41.9	61.4	93.6	96.2	109	104	113	86.7	91.2	121	96.9	−1.0	53.0	69.3	−1.0	−1.0	−1.0
20	34.6	56.2	56.4	110	94.6	127	82.5	154	113	119	67.0	101	196	59.1	34.3	−1.0	−1.0	−1.0
16	30.9	44.6	41.7	133	119	116	123	132	160	139	−1.0	103	190	35.3	31.4	−1.0	−1.0	−1.0
12	44.7	43.0	−1.0	105	−1.0	−1.0	−1.0	−1.0	−1.0	−1.0	−1.0	−1.0	−1.0	55.5	35.6	−1.0	−1.0	−1.0
8	−1.0	−1.0	−1.0	−1.0	−1.0	−1.0	−1.0	−1.0	−1.0	−1.0	−1.0	−1.0	−1.0	134	−1.0	−1.0	−1.0	−1.0

Table 7
Water vapor mixing (ppmv) profiles (aeroid altitudes): L_s=320–360°.

Alt	Latitude																	
(km)	−85	−75	−65	−55	−45	−35	−25	−15	−5	5	15	25	35	45	55	65	75	85
52	3.9	5.4	10.9	11.7	−1.0	−1.0	26.4	66.6	39.7	−1.0	29.3	22.3	27.4	7.3	−1.0	−1.0	−1.0	−1.0
48	−1.0	7.9	12.1	14.7	−1.0	19.6	−1.0	34.9	43.6	−1.0	−1.0	55.5	33.2	12.9	−1.0	2.7	−1.0	−1.0
44	−1.0	−1.0	24.3	−1.0	−1.0	−1.0	−1.0	−1.0	22.7	−1.0	24.6	−1.0	31.7	30.3	−1.0	1.0	−1.0	−1.0
40	6.2	6.5	21.7	−1.0	−1.0	−1.0	78.0	−1.0	41.1	−1.0	25.4	50.5	−1.0	−1.0	−1.0	2.0	−1.0	−1.0
36	−1.0	−1.0	26.3	−1.0	−1.0	−1.0	33.6	−1.0	50.7	−1.0	−1.0	−1.0	−1.0	41.1	−1.0	6.3	−1.0	−1.0
32	−1.0	−1.0	110	−1.0	111	−1.0	90.5	−1.0	87.4	−1.0	52.6	−1.0	99.4	25.8	−1.0	12.0	−1.0	−1.0
28	92.6	158	275	176	59.5	−1.0	−1.0	−1.0	71.2	−1.0	70.5	−1.0	−1.0	111	−1.0	17.9	−1.0	−1.0
24	83.3	216	218	121	47.7	−1.0	98.6	−1.0	105	−1.0	89.6	−1.0	61.4	98.2	−1.0	9.6	−1.0	−1.0
20	49.4	120	127	92.4	48.4	−1.0	106	−1.0	−1.0	−1.0	112	−1.0	−1.0	69.2	−1.0	14.0	−1.0	−1.0
16	49.5	83.4	78.0	−1.0	−1.0	−1.0	−1.0	−1.0	−1.0	−1.0	−1.0	−1.0	−1.0	62.9	−1.0	16.2	−1.0	−1.0
12	−1.0	−1.0	−1.0	−1.0	−1.0	−1.0	−1.0	−1.0	−1.0	−1.0	−1.0	−1.0	−1.0	102	−1.0	2.5	−1.0	−1.0
8	−1.0	−1.0	−1.0	−1.0	−1.0	−1.0	−1.0	−1.0	−1.0	−1.0	−1.0	−1.0	−1.0	−1.0	−1.0	−1.0	−1.0	−1.0

References

Altieri, F., Zasova, L., D'Aversa, E., Bellucci, G., Carrozzo, F.G., Gondet, B., Bibring, J.-P., 2009. On $_2$ 1.27 μm emission maps as derived from OMEGA/MEx data. Icarus 204, 499–511. doi:10.1016/j.icarus.2009.07.022.

Barth, C.A., Hord, C.W., Stewart, A.I., Lane, A.L., Dick, M.L., Anderson, G.P., 1973. Mariner 9 ultraviolet spectrometer experiment: seasonal variation of ozone on Mars. Science 179, 795–796. doi:10.1126/science.179.4075.795.

Berk, A.L., Bernstein, S., Anderson, G.P., Acharya, P.K., Robertson, D.C., Chetwynd, J.H., Adler-Golden, S.M., 1998. MODTRAN cloud and multiple scattering upgrades with application to AVRIS. Remote Sens. Environ. 65, 367–375.

Bertaux, J.L., Gondet, B., Lefèvre, F., Bibring, J.P., Montmessin, F., 2012. First detection of o_2 1.27 μm nightglow emission at mars with OMEGA/MEX and comparison with general circulation model predictions. J. Geophys. Res. (Planets) 117 (E16), 0. doi:10.1029/2011JE003890.

Burkholder, J.B., Sander, S.P., Abbatt, J., Barker, J.R., Huie, R.E., Kolb, C.E., Kurylo, M.J., Orkin, V.L., Wilmouth, D.M., Wine, P.H., 2015. Chemical Kinetics and Photochemical Data for Use in Atmospheric Studies. Technical Report. Jet Propulsion Laboratory, Pasadena, California. Evaluation No 18, Publication 15-10.

Chaufray, J.-Y., Gonzalez-Galindo, F., Forget, F., Lopez-Valverde, M.A., Leblanc, F., Modolo, R., Hess, S., 2015. Variability of the hydrogen in the martian upper atmosphere as simulated by a 3D atmosphere-exosphere coupling. Icarus 245, 282–294. doi:10.1016/j.icarus.2014.08.038.

Clancy, R.T., Grossman, A.W., Wolff, M.J., James, P.B., Rudy, D.J., Billawala, Y.N., Sandor, B.J., Lee, S.W., Muhleman, D.O., 1996. Water vapor saturation at low altitudes around Mars aphelion: A key to Mars climate? Icarus 122, 36–62. doi:10.1006/icar.1996.0108.

Clancy, R.T., Nair, H., 1996. Annual (perihelion-aphelion) cycles in the photochemical behavior of the global Mars atmosphere. JGR 101, 12785–12790. doi:10.1029/96JE00836.

Clancy, R.T., Sandor, B.J., García-Muñoz, A., Lefèvre, F., Smith, M.D., Wolff, M.J., Montmessin, F., Murchie, S.L., Nair, H., 2013. First detection of Mars atmospheric hydroxyl: CRISM Near-IR measurement versus LMD GCM simulation of OH Meinel band emission in the Mars polar winter atmosphere. Icarus 226, 272–281. doi:10.1016/j.icarus.2013.05.035.

Clancy, R.T., Sandor, B.J., Wolff, M.J., Christensen, P.R., Smith, M.D., Pearl, J.C., Conrath, B.J., Wilson, R.J., 2000. An intercomparison of ground-based millimeter, MGS TES, and Viking atmospheric temperature measurements: Seasonal and interannual variability of temperatures and dust loading in the global Mars atmosphere. JGR 105, 9553–9572. doi:10.1029/1999JE001089.

Clancy, R.T., Sandor, B.J., Wolff, M.J., Smith, M.D., Lefèvre, F., Madeleine, J.-B., Forget, F., Murchie, S.L., Seelos, F.P., Seelos, K.D., Nair, H.A., Toigo, A.D., Humm, D., Kass, D.M., Kleinböhl, A., Heavens, N., 2012. Extensive MRO CRISM observations of 1.27 μm O_2 airglow in Mars polar night and their comparison to MRO MCS temperature profiles and LMD GCM simulations. J. Geophys. Res. (Planets) 117 (E16), 0. doi:10.1029/2011JE004018.

Clancy, R.T., Sandor, B.J., Wolff, M.J., Smith, M.D., Lefèvre, F., Madeleine, J.-B., Forget, F., Murchie, S.L., Seelos, F.P., Seelos, K.D., Nair, H.A., Toigo, A.D., Humm, D., Kass, D.M., Kleinböhl, A., Heavens, N., 2013. Correction to extensive MRO CRISM observations of 1.27 μm o_2 airglow in mars polar night and their comparison to MRO MCS temperature profiles and LMD GCM simulations. J. Geophys. Res. (Planets) 118, 1148–1154. doi:10.1002/jgre.20073.

Clancy, R.T., Smith, M., Lefvère, F., Sandor, B., Wolff, M., McConnochie, T., Seelos, K., Nair, H., Toigo, A., Murchie, S., 2015. CRISM limb observations of coincident CO_2 ice clouds and O_2 emission in the Mars equatorial mesosphere. In: AAS/Division for Planetary Sciences Meeting Abstracts. In: AAS/Division for Planetary Sciences Meeting Abstracts, 47, p. 401.07.

Clancy, R.T., Wolff, M.J., Christensen, P.R., 2003. Mars aerosol studies with the MGS TES emission phase function observations: optical depths, particle sizes, and ice cloud types versus latitude and solar longitude. J. Geophys. Res. (Planets) 108, 5098. doi:10.1029/2003JE002058.

Clancy, R.T., Wolff, M.J., James, P.B., 1999. Minimal aerosol loading and global increases in atmospheric ozone during the 1996–1997 Martian Northern spring season. Icarus 138, 49–63. doi:10.1006/icar.1998.6059.

Clancy, R.T., Wolff, M.J., Lefèvre, F., Cantor, B.A., Malin, M.C., Smith, M.D., 2016. Daily global mapping of Mars ozone column abundances with MARCI UV band imaging. Icarus 266, 112–133. doi:10.1016/j.icarus.2015.11.016.

Coman, E.I., Arvidson, R.E., Stein, N., Murchie, S.L., McGovern, A., Seelos, K.D., Seelos, F.P., Humm, D.C., 2013. New CRISM along-track oversampled observations and implications for spectral mapping at fine spatial scales. AGU Fall Meeting Abstracts.

Encrenaz, T., Fouchet, T., Melchiorri, R., Drossart, P., Gondet, B., Langevin, Y., Bibring, J.-P., Forget, F., Bézard, B., 2006. Seasonal variations of the martian CO over hellas as observed by OMEGA/Mars express. Astron. Astrophys. 459, 265–270. doi:10.1051/0004-6361:20065586.

Encrenaz, T., Greathouse, T.K., Lefèvre, F., Montmessin, F., Forget, F., Fouchet, T., DeWitt, C., Richter, M.J., Lacy, J.H., Bézard, B., Atreya, S.K., 2015. Seasonal variations of hydrogen peroxide and water vapor on Mars: further indications of heterogeneous chemistry. Astron. Astrophys. 578, A127. doi:10.1051/0004-6361/201425448.

Encrenaz, T., Greathouse, T.K., Richter, M.J., Bézard, B., Fouchet, T., Lefèvre, F., Montmessin, F., Forget, F., Lebonnois, S., Atreya, S.K., 2008. Simultaneous mapping of H_2O and H_2O_2 on Mars from infrared high-resolution imaging spectroscopy. Icarus 195, 547–556. doi:10.1016/j.icarus.2008.01.022.

Farmer, C.B., Davies, D.W., Holland, A.L., Laporte, D.D., Doms, P.E., 1977. Mars - Water vapor observations from the viking orbiters. J. Geophys. Res. (Planets) 82, 4225–4248. doi:10.1029/JS082i028p04225.

Fast, K., Kostiuk, T., Espenak, F., Annen, J., Buhl, D., Hewagama, T., A'Hearn, M.F., Zipoy, D., Livengood, T.A., Sonnabend, G., Schmülling, F., 2006. Ozone abundance on mars from infrared heterodyne spectra. i. acquisition, retrieval, and anticorrelation with water vapor. Icarus 181, 419–431. doi:10.1016/j.icarus.2005.12.001.

Fedorova, A., Korablev, O., Perrier, S., Bertaux, J.-L., Lefèvre, F., Rodin, A., 2006. Observation of O_2 1.27 μm dayglow by SPICAM IR: seasonal distribution for the first martian year of Mars express. J. Geophys. Res. (Planets) 111, 9. doi:10.1029/2006JE002694.

Fedorova, A.A., Lefèvre, F., Guslyakova, S., Korablev, O., Bertaux, J.-L., Montmessin, F., Reberac, A., Gondet, B., 2012. The o_2 nightglow in the martian atmosphere by SPICAM onboard of Mars-Express. Icarus 219, 596–608. doi:10.1016/j.icarus.2012.03.031.

Fouchet, T., Lellouch, E., Ignatiev, N.I., Forget, F., Titov, D.V., Tschimmel, M., Montmessin, F., Formisano, V., Giuranna, M., Maturilli, A., Encrenaz, T., 2007. Martian water vapor: Mars Express PFS/LW observations. Icarus 190, 32–49. doi:10.1016/j.icarus.2007.03.003.

Gagné, M.-E., Bertaux, J.-L., González-Galindo, F., Melo, S.M.L., Montmessin, F., Strong, K., 2013. New nitric oxide (NO) nightglow measurements with SPICAM/MEx as a tracer of mars upper atmosphere circulation and comparison with LMD-MGCM model prediction: evidence for asymmetric hemispheres. J. Geophys. Res. (Planets) 118, 2172–2179. doi:10.1002/jgre.20165.

Gagné, M.-È., Melo, S.M.L., Lefèvre, F., González-Galindo, F., Strong, K., 2012. Modeled O_2 airglow distributions in the Martian atmosphere. J. Geophys. Res. (Planets) 117, E06005. doi:10.1029/2011JE003901.

Gérard, J.-C., Soret, L., Migliorini, A., Piccioni, G., 2013. Oxygen nightglow emissions of Venus: vertical distribution and collisional quenching. Icarus 223, 602–608. doi:10.1016/j.icarus.2012.11.019.

González-Galindo, F., Chaufray, J.-Y., López-Valverde, M.A., Gilli, G., Forget, F., Leblanc, F., Modolo, R., Hess, S., Yagi, M., 2013. Three-dimensional Martian ionosphere model: I. The photochemical ionosphere below 180 km. J. Geophys. Res. (Planets) 118, 2105–2123. doi:10.1002/jgre.20150.

Guslyakova, S., Fedorova, A., Lefèvre, F., Korablev, O., Montmessin, F., Trokhimovskiy, A., Bertaux, J.L., 2016. Long-term nadir observations of the O_2 dayglow by SPICAM IR. Planet. Space Sci. 122, 1–12. doi:10.1016/j.pss.2015.12.006.

Guslyakova, S., Fedorova, A.A., Lefèvre, F., Korablev, O.I., Montmessin, F., Bertaux, J.-L., 2014. $O_2(a^1\Delta_g)$ dayglow limb observations on Mars by SPICAM IR on Mars-Express and connection to water vapor distribution. Icarus 239, 131–140. doi:10.1016/j.icarus.2014.05.040.

Haberle, R.M., Montmessin, F., Kahre, M.A., Hollingsworth, J.L., Schaeffer, J., Wolff, M.J., Wilson, R.J., 2011. Radiative effects of water ice clouds on the Martian seasonal water cycle. In: Forget, F., Millour, E. (Eds.), Mars Atmosphere: Modelling and observation, pp. 223–226.

Hinson, D.P., Wilson, R.J., 2004. Temperature inversions, thermal tides, and water ice clouds in the Martian tropics. J. Geophys. Res. (Planets) 109, 1002. doi:10.1029/2003JE002129.

Krasnopolsky, V.A., 2003. Mapping of Mars O_2 1.27 μm dayglow at four seasonal points. Icarus 165, 315–325. doi:10.1016/S0019-1035(03)00214-8.

Krasnopolsky, V.A., 2007. Long-term spectroscopic observations of Mars using IRTF/CSHELL: mapping of o $_2$ dayglow, CO, and search for CH $_4$. Icarus 190, 93–102. doi:10.1016/j.icarus.2007.02.014.

Krasnopolsky, V.A., 2009. Seasonal variations of photochemical tracers at low and middle latitudes on Mars: observations and models. Icarus 201, 564–569. doi:10.1016/j.icarus.2009.01.017.

Krasnopolsky, V.A., Bjoraker, G.L., 2000. Mapping of Mars $O_2(^1\Delta)$ dayglow. J. Geophys. Res. 105, 20179–20188. doi:10.1029/2000JE001239.

Lafferty, W.J., Solodov, A.M., Lugez, C.L., Fraser, G.T., 1998. Rotational line strengths and self-Pressure-Broadening coefficients for the 1.27- μm, $a^1\triangle_g$ - $x^3\Sigma_g^-$, $\nu = 0$-0 band of o_2. Appl. Opt. 37, 2264–2270. doi:10.1364/AO.37.002264.

Lebonnois, S., Quémerais, E., Montmessin, F., Lefèvre, F., Perrier, S., Bertaux, J.-L., Forget, F., 2006. Vertical distribution of ozone on mars as measured by SPICAM/mars express using stellar occultations. J. Geophys. Res. (Planets) 111, 9. doi:10.1029/2005JE002643.

Lefèvre, F., Bertaux, J.-L., Clancy, R.T., Encrenaz, T., Fast, K., Forget, F., Lebonnois, S., Montmessin, F., Perrier, S., 2008. Heterogeneous chemistry in the atmosphere of Mars. Nature 454, 971–975. doi:10.1038/nature07116.

Lefèvre, F., Forget, F., 2009. Observed variations of methane on Mars unexplained by known atmospheric chemistry and physics. Nature 460, 720–723. doi:10.1038/nature08228.

Lefèvre, F., Lebonnois, S., Montmessin, F., Forget, F., 2004. Three-dimensional modeling of ozone on Mars. J. Geophys. Res. (Planets) 109 (E18), 7004. doi:10.1029/2004JE002268.

Lefèvre, F., Montmessin, F., Schneider, N.M., Stewart, A.I., Deighan, J., McClintock, W.E., Clarke, J.T., Holsclaw, G.M., Jakosky, B.M., 2015. Ozone mapping on Mars: First results from MAVEN IUVS. In: Lunar and Planetary Science Conference, 46.

Lefèvre, F., Trokhimovsky, A., Fedorova, A., Bertaux, J.-L., Montmessin, F., 2015. Simultaneous satellite observations of ozone and water vapor on mars. Icarus. in preparation

Leiss, A., Schurath, U., Becker, K.H., Fink, E.H., 1978. Reviewed quenching rate constants for metastable oxygen molecules $o_2(a^1\triangle_g)$. J. Photochem. 8, 211–214.

Madeleine, J.-B., Forget, F., Millour, E., Navarro, T., Spiga, A., 2012. The influence of radiatively active water ice clouds on the martian climate. Geophys. Res. Lett. 39, 23202. doi:10.1029/2012GL053564.

Maltagliati, L., Montmessin, F., Fedorova, A., Korablev, O., Forget, F., Bertaux, J.-L., 2011. Evidence of water vapor in excess of saturation in the atmosphere of mars. Science 333, 1868. doi:10.1126/science.1207957.

Maltagliati, L., Montmessin, F., Korablev, O., Fedorova, A., Forget, F., Määttänen, A., Lefèvre, F., Bertaux, J.-L., 2013. Annual survey of water vapor vertical distribution and water-aerosol coupling in the martian atmosphere observed by SPICAM/MEx solar occultations. Icarus 223, 942–962. doi:10.1016/j.icarus.2012.12.012.

McCleese, D.J., Heavens, N.G., Schofield, J.T., Abdou, W.A., Bandfield, J.L., Calcutt, S.B., Irwin, P.G.J., Kass, D.M., Kleinböhl, A., Lewis, S.R., Paige, D.A., Read, P.L., Richardson, M.I., Shirley, J.H., Taylor, F.W., Teanby, N., Zurek, R.W., 2010. Structure and dynamics of the martian lower and middle atmosphere as observed by the Mars climate sounder: seasonal variations in zonal mean temperature, dust, and water ice aerosols. J. Geophys. Res. (Planets) 115 (E14), 12016. doi:10.1029/2010JE003677.

McElroy, M.B., Donahue, T.M., 1972. Stability of the martian atmosphere. Science 177, 986–988. doi:10.1126/science.177.4053.986.

Montabone, L., Forget, F., Millour, E., Wilson, R.J., Lewis, S.R., Cantor, B.A., Kass, D., Kleinböhl, A., Lemmon, M., Smith, M.D., Wolff, M.J., 2014. Eight-year climatology of dust optical depth on Mars. ArXiv e-prints 1409.4841.

Montmessin, F., Forget, F., Rannou, P., Cabane, M., Haberle, R.M., 2004. Origin and role of water ice clouds in the martian water cycle as inferred from a general circulation model. J. Geophys. Res. (Planets) 109, 10004. doi:10.1029/2004JE002284.

Montmessin, F., Lefèvre, F., 2013. Transport-driven formation of a polar ozone layer on Mars. Nat. Geosci. 6, 930–933. 10.1038/ngeo1957

Moudden, Y., McConnell, J.C., 2007. Three-dimensional on-line chemical modeling in a Mars general circulation model. Icarus 188, 18–34. doi:10.1016/j.icarus.2006.11.005.

Murchie, S., Arvidson, R., Bedini, P., Beisser, K., Bibring, J.-P., Bishop, J., Boldt, J., Cavender, P., Choo, T., Clancy, R.T., Darlington, E.H., Des Marais, D., Espiritu, R., Fort, D., Green, R., Guinness, E., Hayes, J., Hash, C., Heffernan, K., Hemmler, J., Heyler, G., Humm, D., Hutcheson, J., Izenberg, N., Lee, R., Lees, J., Lohr, D., Malaret, E., Martin, T., McGovern, J.A., McGuire, P., Morris, R., Mustard, J., Pelkey, S., Rhodes, E., Robinson, M., Roush, T., Schaefer, E., Seagrave, G., Seelos, F., Silverglate, P., Slavney, S., Smith, M., Shyong, W.-J., Strohbehn, K., Taylor, H., Thompson, P., Tossman, B., Wirzburger, M., Wolff, M., 2007. Compact reconnaissance imaging spectrometer for Mars (CRISM) on Mars reconnaissance orbiter (MRO). J. Geophys. Res. (Planets) 112 (E11), 5. doi:10.1029/2006JE002682.

Murchie, S.L., Mustard, J.F., Ehlmann, B.L., Milliken, R.E., Bishop, J.L., McKeown, N.K., Noe Dobrea, E.Z., Seelos, F.P., Buczkowski, D.L., Wiseman, S.M., Arvidson, R.E., Wray, J.J., Swayze, G., Clark, R.N., Des Marais, D.J., McEwen, A.S., Bibring, J.-P., 2009. A synthesis of martian aqueous mineralogy after 1 Mars year of observations from the Mars reconnaissance orbiter. J. Geophys. Res. (Planets) 114 (E13), 0. doi:10.1029/2009JE003342.

Navarro, T., Madeleine, J.-B., Forget, F., Spiga, A., Millour, E., Montmessin, F., Määttänen, A., 2014. Global climate modeling of the martian water cycle with improved microphysics and radiatively active water ice clouds. J. Geophys. Res. (Planets) 119, 1479–1495. doi:10.1002/2013JE004550.

Neary, L., Daerden, F., 2013. Modelling martian atmospheric chemistry with GEM–Mars. In: European Planetary Science Congress 2013, held 8–13 September in London, UK., 8, pp. EPSC2013–399.

Novak, R.E., Mumma, M.J., DiSanti, M.A., Dello Russo, N., Magee-Sauer, K., 2002. Mapping of ozone and water in the atmosphere of Mars near the 1997 aphelion. Icarus 158, 14–23. doi:10.1006/icar.2002.6863.

Noxon, J.F., Traub, W.A., Carleton, N.P., Connes, P., 1976. Detection of O2 dayglow emission from Mars and the Martian ozone abundance. Asrophys. J. 207, 1025–1035. doi:10.1086/154572.

Parkinson, T.D., Hunten, D.M., 1972. Spectroscopy and aeronomy of o_2 on Mars.. J. Atmos. Sci. 29, 1380–1390. doi:10.1175/1520-0469.

Perrier, S., Bertaux, J.L., Lefèvre, F., Lebonnois, S., Korablev, O., Fedorova, A., Montmessin, F., 2006. Global distribution of total ozone on Mars from SPICAM/MEX UV measurements. J. Geophys. Res. (Planets) 111, 9. doi:10.1029/2006JE002681.

Press, W.H., Teukolsky, S.A., Vetterling, W.T., Flannery, B.P., 1992. Numerical Recipes in FORTRAN. The Art of Scientific Computing, second ed. Cambridge: University Press.

Richardson, M.I., Wilson, R.J., 2002. Investigation of the nature and stability of the martian seasonal water cycle with a general circulation model. J. Geophys. Res. (Planets) 107. doi:10.1029/2001JE001536. 7–1.

Rothman, L.S., Gordon, I.E., Barbe, A., Benner, D.C., Bernath, P.F., Birk, M., Boudon, V., Brown, L.R., Campargue, A., Champion, J.-P., Chance, K., Coudert, L.H., Dana, V., Devi, V.M., Fally, S., Flaud, J.-M., Gamache, R.R., Goldman, A., Jacquemart, D., Kleiner, I., Lacome, N., Lafferty, W.J., Mandin, J.-Y., Massie, S.T., Mikhailenko, S.N., Miller, C.E., Moazzen-Ahmadi, N., Naumenko, O.V., Nikitin, A.V., Orphal, J., Perevalov, V.I., Perrin, A., Predoi-Cross, A., Rinsland, C.P., Rotger, M., Šimečková, M., Smith, M.A.H., Sung, K., Tashkun, S.A., Tennyson, J., Toth, R.A., Vandaele, A.C., Vander Auwera, J., 2009. The HITRAN 2008 molecular spectroscopic database. JQSRT 110, 533–572. doi:10.1016/j.jqsrt.2009.02.013.

Rothman, L.S., Jacquemart, D., Barbe, A., Chris Benner, D., Birk, M., Brown, L.R., Carleer, M.R., Chackerian, C., Chance, K., Coudert, L.H., Dana, V., Devi, V.M., Flaud, J.-M., Gamache, R.R., Goldman, A., Hartmann, J.-M., Jucks, K.W., Maki, A.G., Mandin, J.-Y., Massie, S.T., Orphal, J., Perrin, A., Rinsland, C.P., Smith, M.A.H., Tennyson, J., Tolchenov, R.N., Toth, R.A., Vander Auwera, J., Varanasi, P., Wagner, G., 2005. The HITRAN 2004 molecular spectroscopic database. J. Quant. Spectrosc. Radiat. Transfer 96, 139–204. doi:10.1016/j.jqsrt.2004.10.008.

Smith, M.D., 2004. Interannual variability in TES atmospheric observations of Mars during 1999-2003. Icarus 167, 148–165. doi:10.1016/j.icarus.2003.09.010.

Smith, M.D., Wolff, M.J., Clancy, R.T., 2011. Vertical distribution of aerosols and water vapor using CRISM limb observations. In: Forget, F., Millour, E. (Eds.), Mars Atmosphere: Modelling and observation, pp. 188–190.

Smith, M.D., Wolff, M.J., Clancy, R.T., Kleinböhl, A., Murchie, S.L., 2013. Vertical distribution of dust and water ice aerosols from CRISM limb-geometry observations. J. Geophys. Res. (Planets) 118, 321–334. doi:10.1002/jgre.20047.

Smith, M.D., Wolff, M.J., Clancy, R.T., Murchie, S.L., 2009. Compact Reconnaissance Imaging Spectrometer observations of water vapor and carbon monoxide. J. Geophys. Res. (Planets) 114 (E13), 0. doi:10.1029/2008JE003288.

Spurr, R., 2002. Simultaneous derivation of intensities and weighting functions in a general pseudo-spherical discrete ordinate radiative transfer treatment. J. Quant. Spectrosc. Radiat. Trans. 75, 129–175. doi:10.1016/S0022-4073(01)00245-X.

Stamnes, K., Tsay, S.-C., Jayaweera, K., Wiscombe, W., 1988. Numerically stable algorithm for discrete-ordinate-method radiative transfer in multiple scattering and emitting layered media. Appl. Opt. 27, 2502–2509. doi:10.1364/AO.27.002502.

Steele, L.J., Lewis, S.R., Patel, M.R., Montmessin, F., Forget, F., Smith, M.D., 2014. The seasonal cycle of water vapour on mars from assimilation of thermal emission spectrometer data. Icarus 237, 97–115. doi:10.1016/j.icarus.2014.04.017.

Thomas, G.E., Stamnes, K., 2002. Radiative Transfer in the Atmosphere and Ocean. Cambridge University Press.

Trokhimovskiy, A., Fedorova, A., Korablev, O., Montmessin, F., Bertaux, J.-L., Rodin, A., Smith, M.D., 2015. Mars' water vapor mapping by the SPICAM IR spectrometer: five martian years of observations. Icarus 251, 50–64. doi:10.1016/j.icarus.2014.10.007.

Urata, R.A., Toon, O.B., 2013. Simulations of the martian hydrologic cycle with a general circulation model: implications for the ancient martian climate. Icarus 226, 229–250. doi:10.1016/j.icarus.2013.05.014.

Whitney, B.A., Wolff, M.J., Clancy, R.T., 1999. Monte Carlo radiation transfer models for Mars. In: The Fifth International Conference on Mars.

Wolff, M.J., Clancy, R.T., 2003. Constraints on the size of martian aerosols from thermal emission spectrometer observations. J. Geophys. Res.(Planets) 108, 5097. doi:10.1029/2003JE002057.

Wolff, M.J., Clancy, R.T., Cantor, B.A., 2010. Mapping water ice clouds and ozone on Mars with MRO/MARCI. In: AAS/Division for Planetary Sciences Meeting Abstracts #42. In: Bulletin of the American Astronomical Society, 42, p. 1028.

Wolff, M.J., Smith, M.D., Clancy, R.T., Arvidson, R., Kahre, M., Seelos, F., Murchie, S., Savijärvi, H., 2009. Wavelength dependence of dust aerosol single scattering albedo as observed by the compact reconnaissance imaging spectrometer. J. Geophys. Res. (Planets) 114 (E13), 0. doi:10.1029/2009JE003350.

Wolff, M.J., Smith, M.D., Clancy, R.T., Spanovich, N., Whitney, B.A., Lemmon, M.T., Bandfield, J.L., Banfield, D., Ghosh, A., Landis, G., Christensen, P.R., Bell, J.F., Squyres, S.W., 2006. Constraints on dust aerosols from the mars exploration rovers using MGS overflights and mini-TES. J. Geophys. Res. (Planets) 111, 12. doi:10.1029/2006JE002786.